Journal of Materials Science & Technology 106 (2022) 195–210

Contents lists available at ScienceDirect

Journal of Materials Science & Technology

journal homepage: www.elsevier.com/locate/jmst

Research Article

Constructing S-scheme 2D/0D g-C_3N_4/TiO_2 NPs/MPs heterojunction with 2D-Ti_3AlC_2 MAX cocatalyst for photocatalytic CO_2 reduction to CO/CH_4 in fixed-bed and monolith photoreactors

Muhammad Tahir[a,b,*], Beenish Tahir[a]

[a] Department of Chemical Engineering, School of Chemical and Energy Engineering, Universiti Teknologi Malaysia, 81310, UTM Johor Bahru, Malaysia
[b] Chemical and Petroleum Engineering Department, UAE University, P.O. Box 15551, Al Ain, United Arab Emirates

ARTICLE INFO

Article history:
Received 23 May 2021
Revised 8 August 2021
Accepted 9 August 2021
Available online 6 October 2021

Keywords:
Photocatalytic CO_2 methanation
Exfoliated 2D MAX Ti_3AlC_2
g-C_3N_4/TiO_2
Fixed-bed reactor, Monolith photoreactor
Solar energy

ABSTRACT

Exfoliated 2D MAX Ti_3AlC_2 conductive cocatalyst anchored with g-C_3N_4/TiO_2 to construct 2D/0D/2D heterojunction has been explored for enhanced CO_2 photoreduction in a fixed-bed and monolith photoreactor. The TiO_2 particle sizes (NPs and MPs) were systematically investigated to determine effective metal-support interaction with faster charge carrier separation among the composite materials. When TiO_2 NPs were anchored with 2D Ti_3AlC_2 MAX structure, 10.44 folds higher CH_4 production was observed compared to anchoring TiO_2 MPs. Maximum CH_4 yield rate of 2103.5 μmol g^{-1} h^{-1} achieved at selectivity 96.59% using ternary g-C_3N_4/TiO_2/Ti_3AlC_2 2D/0D/2D composite which is 2.73 and 7.45 folds higher than using binary g-C_3N_4/Ti_3AlC_2 MAX and TiO_2 NPs/Ti_3AlC_2 samples, respectively. A step-scheme (S-scheme) photocatalytic mechanism operates in this composite, suppressed the recombination of useful electron and holes and provides higher reduction potential for efficient CO_2 conversion to CO and CH_4. More importantly, when light intensity was increased by 5 folds, CH_4 production rate was increased by 3.59 folds under visible light. The performance of composite catalyst was further investigated in a fixed-bed and monolith photoreactor and found monolithic support increased CO production by 2.64 folds, whereas, 53.99 times lower CH_4 production was noticed. The lower photocatalytic activity in a monolith photoreactor was due to lower visible light penetration into the microchannels. Thus, 2D MAX Ti_3AlC_2 composite catalyst can be constructed for selective photocatalytic CO_2 methanation under visible light in a fixed-bed photoreactor.

1. Introduction

The replacing fossil fuels with renewable energy sources and alleviating global warming by utilizing greenhouse gas CO_2 are the two major challneges in the 21st century [1]. Among all, photocatalytic CO_2 reduction to hydrocarbon fuels has gained significant consideration, since it hold promises to solving both the energy and environmental issues [2]. However, efficient CO_2 reduction through artificial photosynthesis is one of the main challenge in the phototechnology, in addition of producing diversity products which include CO, CH_3OH, CH_4, C_2H_5OH and HCHO [3,4]. Therefore, design of advanced semiconductor photocatalysts functional under visible light with high activity and selectivity are highly demanding to reach acceptance level of commercialization.

Among the higher oxidative potential semiconductors, TiO_2 is one of the most widely explored photocatalyst because of its low lost, high photostability and appropriate redox potential for many applications [5]. Nevertheless, pristine TiO_2 has lower photoactivity and products selectivity due to recombination of charge carrier and sluggish response under visible light [6]. The large size TiO_2 particles disfavors to provide larger surface area, lower light harvesting, and slower adsorption of gas molecules, resulting in lower photocatalytic CO_2 reduction efficiency [7]. Loading metals and constructing heterojunction with other semiconductors are among the promising strategies to enhance photocatalytic efficiency of TiO_2. In this view point, Au-CeO coupled with hollow TiO_2 has been reported for photoinduced reduction of CO_2 with selective CO and CH_4 production [8]. Similarly, efficient CO_2 conversion to CH_4 over Cu-doped TiO_2 has been obtained [9]. In many other works, PbO decorated TiO_2 for remarkably enhanced production of CH_4 and CO during CO_2 reduction [10], Pt-doped TiO_2 for the photoreduction of CO_2 to CH_4 [11], WO_3-TiO_2/Cu_2ZnSnS_4 ternary composite with enhanced CO_2 reduction efficiency [12], enhanced CO_2 photoreduction over CdS/TiO_2 for CH_4 production [13] and $ZnFe_2O_4$/TiO_2 hybrid composite for photocatalytic CO_2 reduction to methanol [14], have been reported. All these findings demonstrate that TiO_2 pho-

* Corresponding author.
E-mail address: mtahir@cheme.utm.my (M. Tahir).

https://doi.org/10.1016/j.jmst.2021.08.019
1005-0302/

tocatalytic activity can be stimulated through loading with metals or constructing heterojunctions.

Among the newly emerged semiconductor materials, two dimensional (2D) graphitic carbon nitride (g-C_3N_4) has been widely examined for photocatalytic CO_2 reduction due to its distinct optical characteristics, higher light absorption, and good reduction potential for conversion of CO_2 to several products [15,16]. However, g-C_3N_4 has more recombination of charge carrier, resulting in lower photocatalytic activity [17]. Coupling 2D g-C_3N_4 with TiO_2 NPs and other cocatalysts would be beneficial to construct semiconductor heterojunction with proficient separation of photoinduced charge carrier [18–20]. In this perspective, Mn and Co modified g-C_3N_4 with efficient CO_2 photoreduction to CO and CH_4 has been reported [21]. Enhanced photocatalytic CO_2 reduction was obtained when La was doped with g-C_3N_4 [22]. Similarly, enhanced CO_2 reduction over Cu-NPs loaded CNTs/g-C_3N_4 has been reported due to hindered charges recombination by Cu [23]. Z-scheme heterojunction of Fe_2O_3/g-C_3N_4 with enhanced photocatalytic CO_2 conversion to methanol has been reported [24]. In another development, 2D/2D heterojunction of ZnV_2O_6/g-C_3N_4 was developed to promote charge carrier separation, resulting efficient CO_2 reduction to CH_3OH under visible light [25]. Recently, ultrathin g-C_3N_4-coupled with Au/TiO_2 was investigated and reported efficient visible light induced photocatalytic CO_2 reduction by H_2O as reducing agent [26]. The performance of semiconductors could be further stimulated by constructing heterojunction over low cost and stable 2D structured materials

In the current development, 2D carbon and nitrogen-based materials are under exploration to be used as a cocatalyst in photocatalytic and other applications [27,28]. In this regard, MAX phases have general formula $M_{n+1}AX_n$, where, n=1, 2 or 3; X is either carbon or nitrogen; M is early transition metal and A belongs to group III A or IV A element. MAX belongs to the class of carbide and nitrides family with a laminar hexagonal crystalline structure [29]. They have characteristics of ceramics and metals due to their high thermal stability, high mechanical hardness and good electrical and thermal conductive properties. MAX materials are suitable for several applications such as thermal barriers, high temperature heating elements, and as efficient electrical conductors [30,31]. In the MAX family, two dimensional (2D) titanium aluminum carbide (Ti_3AlC_2) with multilayered structure is very promising due to its good thermal conductivity, and can be used as a cocatalyst with other semiconductors to boost charge carrier separation [32]. Constructing 2D/2D heterojunction has more potential to promote charge carrier separation due to good interaction and surface contacts [33].

Recently, 2D/2D heterojunction of Ti_3C_2 MXene/g-C_3N_4 composite was employed for efficient photocatalytic CO_2 reduction to CO and CH_4. It was observed that 2D Ti_3C_2 efficiently prevent charges recombination rate and enabling proficient photoactivity and productivity [34]. 2D/2D heterojunction of ultrathin MXene/Bi_2WO_6 nanosheets for improved photocatalytic CO_2 reduction has been reported [35]. In another work, MAX-phase Ti_3AlC_2 for improving hydrogen storage properties of MgH_2 was obtained [36]. Similarly, Ti_3AlC_2 anchored over TiO_2/ Ni_2P was investigated for photocatalytic water splitting with efficient hydrogen production [37]. In another development, enhanced charges separation over Ti_3C_2 MXene/TiO_2 NPs composite, resulting in higher photocatalytic activity [38]. TiO_2/Ti_3C_2 MXenes for enhanced photocatalytic CO_2 reduction to fuels has been reported [39]. Ultrathin Ti_3C_2 MXene as cocatalyst anchored with g-C_3N_4 found efficient for visible light driven CO_2 photoreduction [40]. All these findings confirm MAX or MXene as an efficient cocatalyst and would be employed with other semiconductors for promoting photocatalytic activity. However, limited reports are available on the direct use of MAX as cocatalyst or as a mediator in photocatalytic applications.

In addition, the performance of photocatalyst for photocatalytic CO_2 to specific product is entirely dependent on the types of photoreactor employed. In the recent development slurry, fixed-bed and monolith photoreactors are under exploration for the production of CH_3OH, CO and CH_4 under UV and visible light. However, fixed-bed and monolith photoreactors are very promising for CO and CH_4 production under UV light irradiation [41]. Thus, exploring fixed-bed and monolith photoreactor with new developed heterojunction of Ti_3AlC_2 with g-C_3N_4 and dispersed with TiO_2 NPs would be new contribution in the field of photocatalysis and energy applications.

Herein, for the first time, we are utilizing 2D Ti_3AlC_2 MAX as a conductive support to construct step-scheme 2D/0D heterojunction of g-C_3N_4 and TiO_2 NPs heterojunction composite with proficient interaction by optimizing different sizes TiO_2 particles. The TiO_2 NPs dispersed with 2D Ti_3AlC_2 MAX composite showed highest photocatalytic CO_2 reduction efficiency due to good interaction with faster charger carrier separation. When 2D g-C_3N_4 was used as catalyst with 2D Ti_3AlC_2/TiO_2 NPs, a well-designed composite with selective production of CH_4 during photocatalytic CO_2 reduction was achieved. Under simulated solar energy, performance of composite was further enhanced with significant amount of CH_4 production compared to TiO_2 and g-C_3N_4 catalysts. On the basis of engineering approach, fixed-bed and monolith photoreactors performances were further examined and found higher visible light induced CO_2 photoreduction efficiency through fixed bed photoreactor. The findings from this work would be useful to construct highly efficient and selective composite for methane formation under visible light irradiation.

2. Experimental

2.1. Catalyst preparation

2.1.1. Chemicals

The chemicals used for the preparations of catalysts were melamine ($C_3H_6N_6$, MW=126.12 g/mol, purity~99%, Sigma-Aldrich), titanium (IV) isopropoxide (TTIP, tetraisopropyl orthotitanate, $C_{12}H_{28}O_4Ti$, purity ~97%, MW=284.22 g/mol), acetic acid (CH_3COOH, MW=60.05 g/mol, 99.8%), 2-propanol (MW=60.1 g/mol and $CH_2CH(OH)CH_3$, Merck). Besides, titanium aluminum carbide (Ti_3AlC_2) was purchased from China (Famous Chemical) and monoliths of 100 channels per square inch (CPSI 100) were purchased from Pingxiang Meitao, China.

2.1.2. Preparation of g-C_3N_4

The g-C_3N_4 was synthesized using a simple heating method, in which, melamine was heated in a furnace at 550 °C for 2 h under air atmosphere [41]. The ceramic vessel was covered with a lid, where, furnace heating rate of 10 °C min^{-1} was adjusted to achieve temperature of 550 °C. After grinding bulky material, it was dispersed in acetic acid for surface modification and finally washed with DI water and centrifuged to get graphitic carbon nitride (g-C_3N_4).

2.1.3. Preparation of TiO_2 MPs/Ti_3AlC_2 composite

The TiO_2 MPs/Ti_3AlC_2 composite samples were synthesized using a simple impregnation method. TiO_2 MPs (Sigma-Aldrich, anatase) were dispersed in a methanol solution and were stirred well for their uniform suspension [32]. Afterwards, specific amount of exfoliated Ti_3AlC_2 was added into above suspension and stirred for 24 h to get their good interaction. Finally, suspension was oven dried for 24 h at 100 °C to get TiO_2 MPs/Ti_3AlC_2 composite.

2.1.4. Preparation of TiO_2 NPs/Ti_3AlC_2 composite

Sol-gel method was used for fabricating Ti_3AlC_2/TiO_2 NPs composite using TTIP as the precursor. Typically, TTIP of 10 mL dis-

persed in 2-propanol was hydrolyzed using acetic acid (1M) to get titanium sol according to our previous work [42]. In parallel, Ti_3AlC_2 was dispersed in a methanol solution under stirring for 24 h to get exfoliated Ti_3AlC_2 multi-layers. The specific amount of Ti_3AlC_2 were added to above titanium sol under stirring and this process was continued for another 12 h to get thick titanium sol. The sol obtained was oven dried at 100 °C overnight and finally calcined for 2 h at 500 °C to get Ti_3AlC_2 anchored TiO_2 NPs composite. The pristine TiO_2 NPs were synthesized using the same method, but without the addition of Ti_3AlC_2.

2.1.5. Preparation of TiO_2 NPs/Ti_3AlC_2/g-C_3N_4 composites

The g-C_3N_4 coupled TiO_2 and Ti_3AlC_2 composite samples were synthesized using sol-gel method. As discussed above, g-C_3N_4 were obtained through heating of melamine, whereas, exfoliated Ti_3AlC_2 was employed for the preparation of composite samples. Specifically, titanium sol was prepared as discussed above and specific amount of g-C_3N_4 and Ti_3AlC_2 were added into it and was stirred for 24 h to get homogeneous thick sol. The suspension was dried for 24 h at 100 °C and finally calcined for 2 h at 500 °C and named as TiO_2 NPs/Ti_3AlC_2/g-C_3N_4 composite. Similar to composite catalyst, TiO_2 coupled g-C_3N_4 composite was synthesized using sol-gel method without adding Ti_3AlC_2 material.

2.1.6. Preparation of monolithic TiO_2 NPs/Ti_3AlC_2/g-C_3N_4 composites

Monolithic TiO_2-loaded Ti_3AlC_2 and g-C_3N_4 composite was synthesized using modified sol-gel dip-coating approach. Before loading the catalysts over the monolithic surface, monoliths preparation was conducted. The specific sizes monoliths (thickness 2 cm and radius 3 cm) were washed before being loaded with catalyst. The composite sol obtained as discussed above, before drying was placed in a beaker for dip-coating. Before coating, initial weights of the monoliths were calculated and after dip-coating, the final monolith weight was noted. After coating, loaded catalyst was controlled by repeating the same coating procedure. After dip-coating, excess amount of catalyst was removed using hot compressed air with the help of air dryer. Finally, monoliths, after drying at 100 °C for 24 h were calcined for 2 h at 500 °C. The composite obtained was named as monolithic TiO_2/Ti_3AlC_2/g-C_3N_4. The amount of catalyst loaded over the monolithic channels was calculated by subtracting the final weight of monolith from the initial ones. The estimated amount of catalyst loaded was ~250 mg and schematic illustration of composite catalyst preparation is shown in Fig. 1.

2.2. Catalyst characterization

All the catalyst samples were characterized using several analytical techniques. The purity and crystal phases structures were analyzed using XRD (X-ray powder diffraction) with the help of Bruker Advance D8 diffractometer. The Raman analysis was further conducted with the help of HORIBA Scientific Spectrophotometer (laser ~532 nm) to confirm the interaction among the composite materials. The structure and morphology were obtained suing FE-SEM (Scanning electron microscopy, Hitachi SU8020) and HRTEM (High resolution transmission electron microscopy, JEOL JEM-ARM 200F). The chemical composition and elemental states were measured through XPS (X-ray photoelectron Spectroscopy) using Axis Ultra DLD Shimadzu spectrometer. The optical response of the materials was measured through UV-visible diffuse reflectance spectrometer (DRS), using spheres for loading powder samples with (UV-3600 Plus Spectrometer). The PL (photoluminescence) analysis were conducted with HORIBA Scientific spectrometer, laser 325 nm).

2.3. Photoactivity CO_2 reduction set-up and procedure

The experimental set-up for investigating the performance of synthesized photocatalysts for CO_2 reduction in a fixed bed and a monolith photoreactor is shown in Fig. S1. Fig. S1(a) shows the schematic illustration of fixed bed reactor equipped with a glass window, mass flow controllers and online products analysis. A 35 W HID car lamp with intensity 20 mW cm^{-2} was located at the top of quartz glass window and water saturator was connected with the reactor to carry moisture during the CO_2 entering into the reactor. The powder photocatalyst (150 mg) was uniformly dispersed inside the reactor chamber at the bottom surface and the interaction between the reactants, light source and catalyst was only at the external exposed surface area. Before that, reactor was purged before starting CO_2 reduction experiments for 30 min. Afterwards, CO_2 (10 mL min^{-1}, purity~99.99 %), was saturated with water vapors by passing through the water. Feed mixture (CO_2 and H_2O) was constantly flowing for 30 min through the reactor to saturate the catalyst surface before starting the experiment. Before truing on the lamp reactor outlet and inlet valves were closed for batch mode experiments. The schematic of monolith photoreactor experimental set-up has been demonstrated in Fig. S1(b). The reactor chamber was the same as like the fixed bed reactor, however, the catalyst was immobilized over the monolithic channels before inserting into the reactor. All the experimental parameters and operating procedure was similar to fixed bed reactor as discussed above. Two types of light sources i.e., 35 and 300 W having intensities 20 and 100 mW cm^{-2}, respectively, were used. The products were analyzed using GC-TCD/FID connected with capillary column (Carboxen-1010 PLOT).

2.4. Quantum yield and selectivity calculations

In photocatalytic CO_2 reduction applications, the performance of catalysts is greatly altered using different types of light sources and illuminated surface area. This performance is also dependent on the types of photoreactor employed. As the number of electrons used for different products varied based on the types of products such as 2 and 8 electrons would be consumed for the production of one mole of CO and CH_4, respectively. Thus, quantum efficiency analysis is very important to evaluate photocatalytic CO_2 reduction system under different operating conditions. In general, quantum yield (QY) is a measure of production rate of a specific product per unit time to the amount of photon flux consumed in a unit time. This also reflects the efficient production and utilization of electrons and holes during photocatalysis process. The QY for CO and CH_4 was calculated according to Eqs. (1) and (2) [26,43]. The photon flux was estimated using the Eq. (3), which involves the light intensity and wavelength of light irradiation.

$$QY(CO) = \frac{2 \times \text{moles of CO } (\mu\text{mol h}^{-1})}{\text{Photon flux} \times \text{Incident area } (\text{m}^2)} \quad (1)$$

$$QY(CH_4) = \frac{8 \times \text{moles of } CH_4 \ (\mu\text{mol h}^{-1})}{\text{Photon flux} \times \text{Incident area } (\text{m}^2)} \quad (2)$$

$$\text{Photon flux} = \frac{\lambda(m)}{h\nu} \times \text{Intensity}(\text{Wm}^{-2}) \quad (3)$$

where, λ is wavelength of light, h is planks constant (6.62×10^{-34} J) and ν is photon density (3.0×10^8). Finally, electron selectivity towards specific products was calculated based on number of electrons consumed and amount of specific product obtained as

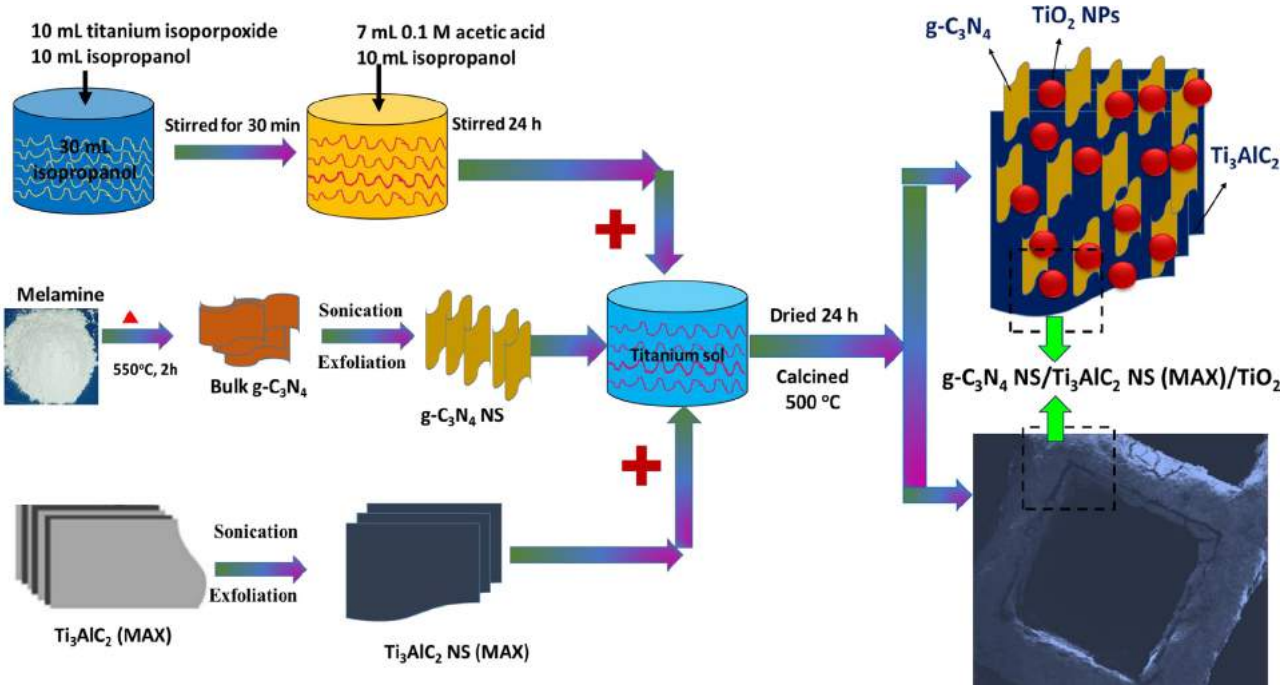

Fig. 1. Schematic illustration for the synthesis of $TiO_2/Ti_3AlC_2/g\text{-}C_3N_4$ and monolithic $TiO_2/Ti_3AlC_2/g\text{-}C_3N_4$ composite samples.

demonstrated in Eqs. (4) and (5) [44].

Selectivity of CO (%)

$$= \frac{2 \times \mathrm{RCO}\ \left(\mu\mathrm{mol\ g^{-1}h^{-1}}\right)}{2 \times \mathrm{RCO}\ \left(\mu\mathrm{mol\ g^{-1}h^{-1}}\right) + 8 \times \mathrm{RCH_4}\ \left(\mu\mathrm{mol\ g^{-1}h^{-1}}\right)} \quad (4)$$

Selectivity of CH_4 (%)

$$= \frac{8 \times \mathrm{RCH_4}\ \left(\mu\mathrm{mol\ g^{-1}h^{-1}}\right)}{2 \times \mathrm{RCO}\ \left(\mu\mathrm{mol\ g^{-1}\ h^{-1}}\right) + 8 \times \mathrm{RCH_4}\left(\mu\mathrm{mol\ g^{-1}\ h^{-1}}\right)} \quad (5)$$

where 2 and 8 are the electrons that would be consumed for CO and CH_4 production, respectively, and RCO and RCH_4 are the production rates of CO and CH_4 during photocatalytic CO_2 reduction with H_2O under visible light irradiation.

3. Results and discussion

3.1. Characterization of catalysts

The crystal structure of the pure and modified samples was determined using XRD analysis as presented in Fig. 2. XRD analysis of TiO_2 NPs, TiO_2 MPs, Ti_3AlC_2 MAX and their composite samples is shown in Fig. 2(a). In both TiO_2 NPs and MPs samples, pure anatase phase was achieved, which confirms their successful fabrication. Similarly, all the peaks of Ti_3AlC_2 are assigned to MAX structure and similarly reported in Ref. [40]. When Ti_3AlC_2 was anchored with TiO_2 MPs through physical mixing method, there was no effect on the crystalline structure. However, crystal size of TiO_2 was further reduced when anchored with Ti_3AlC_2 through sol-gel method. This confirms that sol-gel method is an effective approach to construct well-designed heterojunction with controlled growth of TiO_2 NPs and would be beneficial for promoting charge carrier separation [32].

The lattice structure and phase composition of $g\text{-}C_3N_4$, $g\text{-}C_3N_4$ loadedTiO_2 NPs and 2D MAX Ti_3AlC_2 based photocatalysts were further investigated by XRD patterns and their results are demonstrated in Fig. 2(b). Pure $g\text{-}C_3N_4$ presents two peaks at 2θ of 13.07° and 37.39°, attributed to the (100) and (002) facets of $g\text{-}C_3N_4$. When $g\text{-}C_3N_4$ was loaded with TiO_2 through sol-gel method, TiO_2 crystalline size was reduced, whereas, $g\text{-}C_3N_4$ peaks were not obvious due to its lower crystallinity compared to TiO_2 NPs. A similar trend in reduced crystal size of TiO_2 was obtained with Ti_3AlC_2, which confirms their good interaction. When $g\text{-}C_3N_4$ was anchored with Ti_3AlC_2, all the peaks of both the materials were observed, which confirmed successful synthesis of this composite without any alternation in their structure and phase change. Finally, XRD patterns of $g\text{-}C_3N_4/TiO_2/Ti_3AlC_2$ MAX composite confirms the presence of all the peaks without any alternation in their peak position, which further confirms a successful synthesis of the ternary composite catalyst.

The Raman analysis was performed to estimate the interaction among the materials and their successful fabrication through different methods. Fig. 3(a) shows Raman results of TiO_2 of different sizes and their interaction with Ti_3AlC_2 2D MAX structure. Exfoliated Ti_3AlC_2 reflects vibrational modes at 151.4, 204.56, 265.23, 411.16 and 605.28 cm^{-1}, corresponding to ω_1, ω_2, ω_3, ω_4, and ω_5 characteristics modes of Ti_3AlC_2 MAX phase, confirming the presence of Ti and Al [37]. For TiO_2 NPs, characteristics modes were appeared at 142.03, 19.49, 394.24, 511.80 and 635.01 cm^{-1}, corresponds to E_{g1}, E_{g2}, B_{1g}, $A_{1g}+B_{1g}$ and A_{g3} modes, confirming successful fabrication of single phase TiO_2 NPs [26]. When TiO_2 NPs and TiO_2 MPs were loaded over the Ti_3AlC_2 surface, band positions were shifted towards higher values, which confirm, successful fabrication of composite.

The structural and vibrational modes of $g\text{-}C_3N_4$, $g\text{-}C_3N_4/Ti_3AlC_2$ MAX and $g\text{-}C_3N_4$ based composites were further analyzed using Raman spectroscopy and the results are presented in Fig. 3(b). Raman modes of pristine $g\text{-}C_3N_4$ confirm successful synthesis of graphitic structure of carbon nitride as similarly observed by XRD analysis [45]. When Ti_3AlC_2 was anchored with Ti_3AlC_2, all the Raman modes were appeared, which confirms their successful fabrication. Comparatively, when TiO_2 was loaded with $g\text{-}C_3N_4/Ti_3AlC_2$ MAX, bands positions were shifted towards higher values, which confirm their good interaction, synthesized through sol-gel method [37]. All these results have good agreement with XRD data and

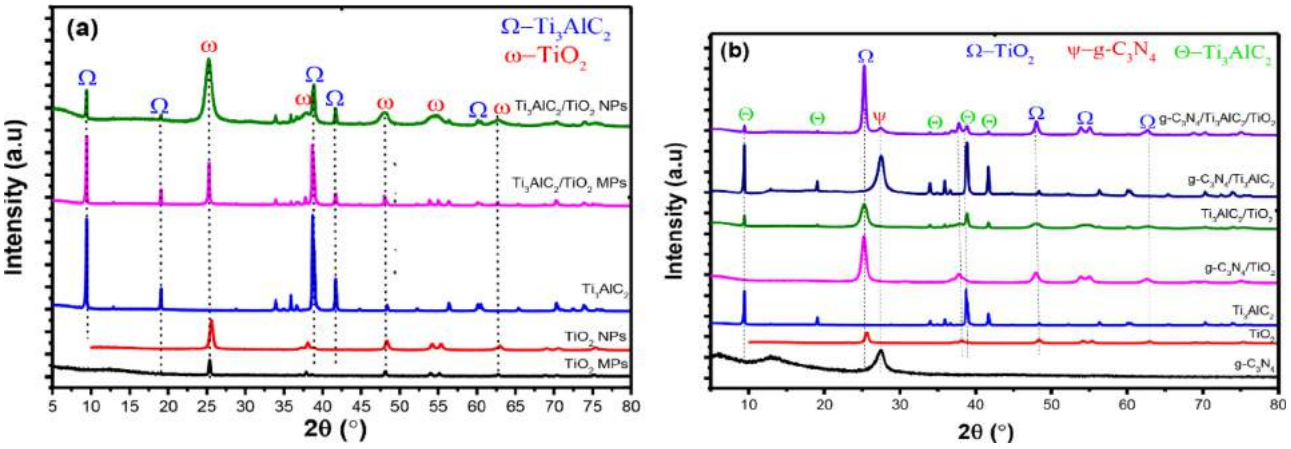

Fig. 2. **(a)** XRD patterns of TiO_2 NPs, TiO_2 MPs, Ti_3AlC_2 MAX, TiO_2 MPs/Ti_3AlC_2 TiO_2 NPs/Ti_3AlC_2 samples; (b) XRD patterns of g-C_3N_4, g-C_3N_4/TiO_2 NPs, g-C_3N_4/Ti_3AlC_2 MAX and g-C_3N_4/TiO_2/Ti_3AlC_2 composite samples.

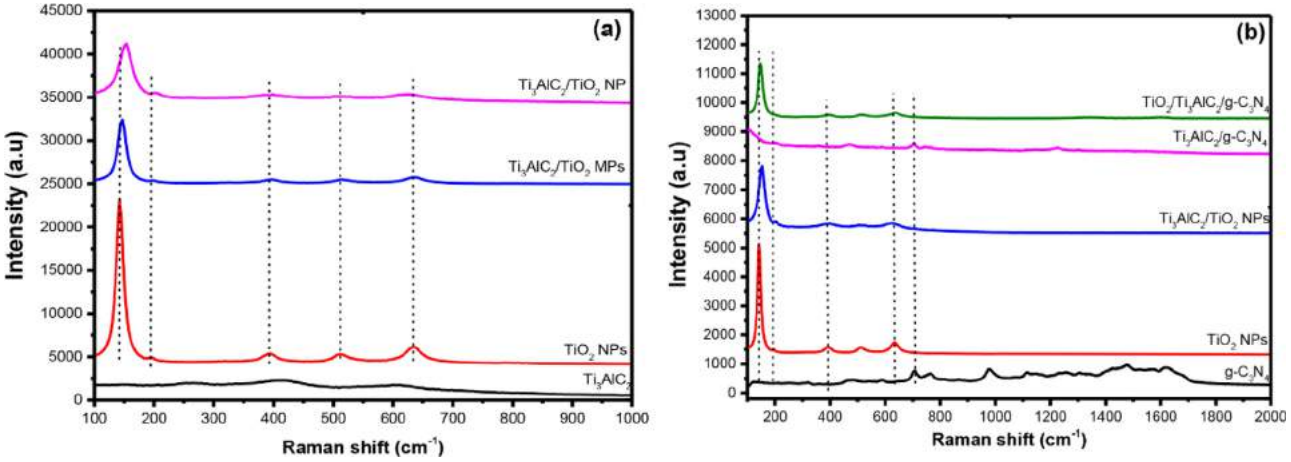

Fig. 3. (a) Raman analysis 2D Ti_3AlC_2 MAX, pristine TiO_2 NPs, Ti_3AlC_2 anchored TiO_2 MPs and Ti_3AlC_2/TiO_2 NPs; (b) Raman patterns of pristine g-C_3N_4, pristine TiO_2 NPs, 2D Ti_3AlC_2 MAX/TiO_2 NPs and g-C_3N_4/TiO_2 NPs/Ti_3AlC_2 MAX composite.

confirm successful fabrication of composite samples without alternation in their phase structure.

The morphology of pristine TiO_2 NPs, pristine TiO_2 MPs and NPs/MPs loaded Ti_3AlC_2 MAX was further investigated using FE-SEM and TEM characterization techniques as shown in Fig. 4. Fig. 4(a) shows large size TiO_2 particles with particle size distribution of 60 to 200 nm with mean 130 nm. Similarly, pristine TiO_2 NPs were obtained using sol-gel method as presented in Fig. 4(b). Obviously smaller sized TiO_2 NPs with size distribution of 12 to 40 nm and mean of 20 nm was observed. The morphology of exfoliated Ti_3AlC_2 multilayers has been illustrated in Fig. 4(c). Evidently, using ultrasonic approach, Ti_3AlC_2 sticky sheets can be exfoliated to get larger exposed surface area. Fig. 4(d) shows the interaction of TiO_2 MPs with 2D Ti_3AlC_2 MAX nanosheets, in which, TiO_2 MPs were distributed over the Ti_3AlC_2 sheets, but their interaction was not very good due to using large size TiO_2 particles. However, a good dispersion with uniform distribution of TiO_2 NPs over the entire surface of 2D Ti_3AlC_2 multilayers was achieved using sol-gel method as demonstrated in Fig. 4(e). All these findings confirm that good distribution and interaction of TiO_2 with Ti_3AlC_2 could be achieved using sol-gel method.

The morphology of TiO_2 NPs loaded 2D Ti_3AlC_2 sheets were further examined using TEM as shown in Fig. 4(f). Obviously, TiO_2 NPs are evenly distributed over the 2D layers of Ti_3AlC_3 with their good interaction. Furthermore, HRTEM images in Fig. 4(g) presents a good interaction with heterojunction formation between the materials, which would be beneficial for promoting photocatalytic activity. The d-spacing in Fig. 4(h-i) of 0.214 and 0.36 nm were obtained for Ti_3AlC_2 and anatase phase TiO_2 NPs. Thus, successful fabrication of 0D TiO_2 NPs/2D Ti_3AlC_2 heterojunction can be developed using ultrasonic assisted sol-gel approach.

Fig. 5 shows morphology of g-C_3N_4, TiO_2 NPs/g-C_3N_4 and TiO_2 NPs/g-C_3N_4 dispersed 2D Ti_3AlC_2 composite samples. SEM image in Fig. 5(a) shows 2D sheets of g-C_3N_4 with wrinkled structure. Fig. 5(b) presents SEM image of TiO_2 NPs/g-C_3N_4 composite synthesized through sol-gel method. Obviously, TiO_2 NPs were uniformly dispersed with 2D g-C_3N_4 sheets, thus, constructing 0D/2D heterojunction. SEM in Fig. 5(c) further shows interaction of 2D g-C_3N_4 with 2D Ti_3AlC_2 to construct 2D/2D heterojunction with good interaction among the two materials. The SEM images for ternary TiO_2 NPs, g-C_3N_4 and Ti_3IAC_2 are shown in Fig. 5(d, e), confirming good interaction among the three materials.

The interaction among the TiO_2/g-C_3N_4 dispersed Ti_3AlC_2 was further confirmed using TEM analysis as presented in Fig. 5(f). Evidently, 2D/2D g-C_3N_4/Ti_3AlC_2 MAX heterojunction was successfully synthesized with their good interaction. Fig. 5(g) presents HRTEM image of the composite, demonstrating good interaction. The d-spacing results in Fig. 5(h-j) further confirms lattice fringes of 0.467, 0.36 and 0.322 nm for Ti_3AlC_2, TiO_2 NPs and g-C_3N_4, respectively. Thus, g-C_3N_4/Ti_3AlC_2 MAX 2D/2D heterojunction dispersed with TiO_2 NPs were successfully fabricated using modified sol-gel method.

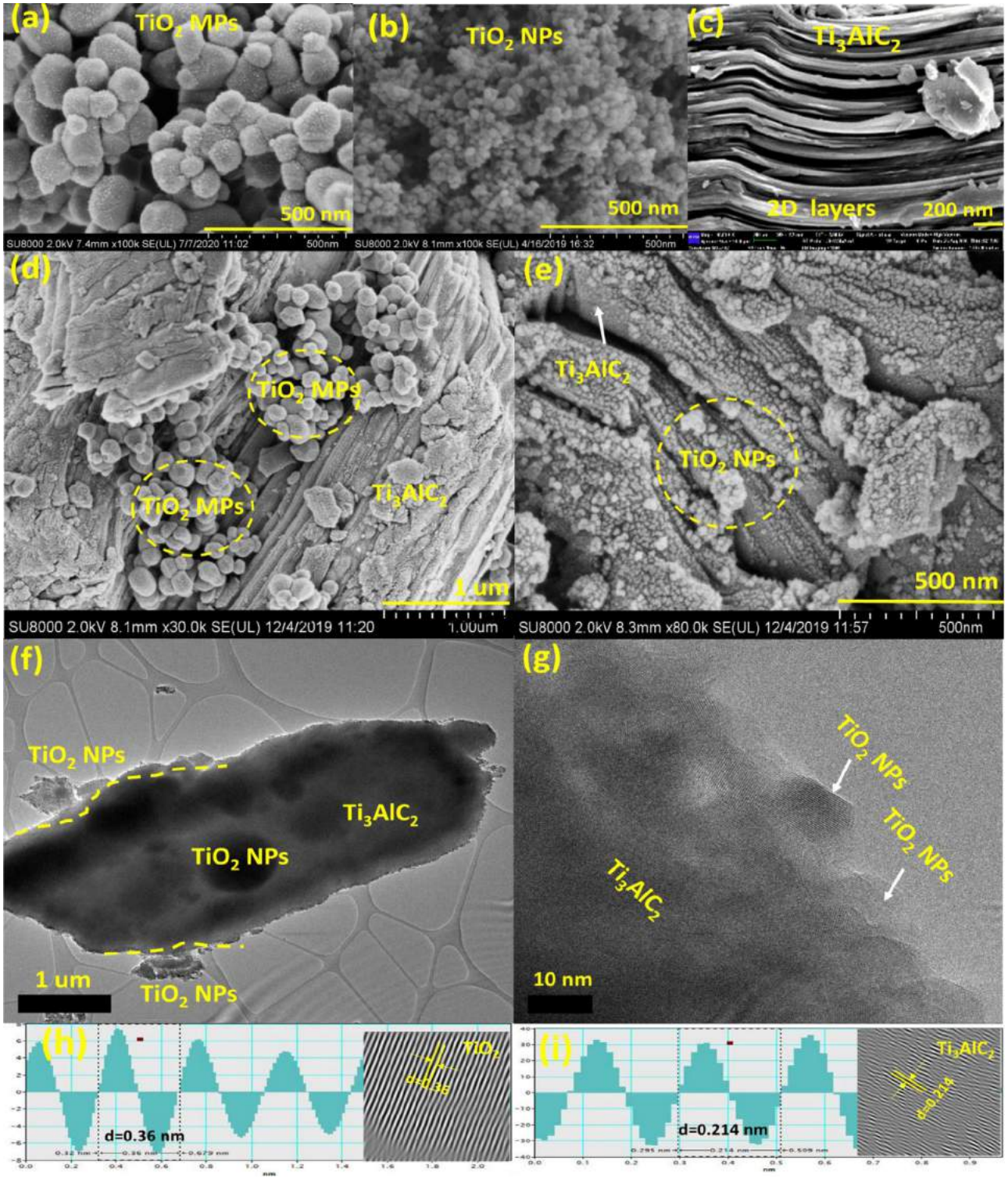

Fig. 4. FESEM analysis of (a) TiO_2 MPs, (b) TiO_2 NPs, (c) exfoliated Ti_3AlC_2, (d, e) TiO_2 MPs/Ti_3AlC_2, (f, g) TiO_2 NPs/Ti_3AlC_2, (h-i) TEM images of TiO_2 NPs/Ti_3AlC_2, (k) HRTEM images of TiO_2 NPs/Ti_3AlC_2 with d-spacing analysis.

The chemical states of surface elements were further explored through X-ray photoelectron spectroscopy (XPS) and the results are demonstrated in Fig. 6. Fig. 6(a) shows XPS plots of Ti 2p of TiO_2, 2D Ti_3AlC_2, TiO_2 loaded Ti_3AlC_2 and g-C_3N_4/TiO_2/Ti_3AlC_2 photocatalysts. For TiO_2 sample, high resolution spectrum presents two peaks located at 458.5 and 464.2 eV, corresponds to Ti $2p_{3/2}$ and Ti $2p_{1/2}$ and confirms the formation of anatase TiO_2. Similarly, in Ti_3AlC_2 sample, binding energies are centered at 453.8, 457.5, 459.9 and 463.9 eV. The binding energies of Ti-C $2p_{3/2}$ and Ti-C $2p_{1/2}$ are positioned at 453.8 and 459.9 eV, respectively. Similarly, peaks at 457.5 and 463.9 eV are ascribed to Ti-O $2p_{3/2}$ and Ti-O $2p_{1/2}$, respectively. XPS spectrum of g-C_3N_4/TiO_2/Ti_3AlC_2 presents three peaks with 461.8, 459.3 and 465.1 eV binding energies, ascribed to Ti-C, Ti $2p_{3/2}$ and Ti $2p_{1/2}$, respectively. It could be seen

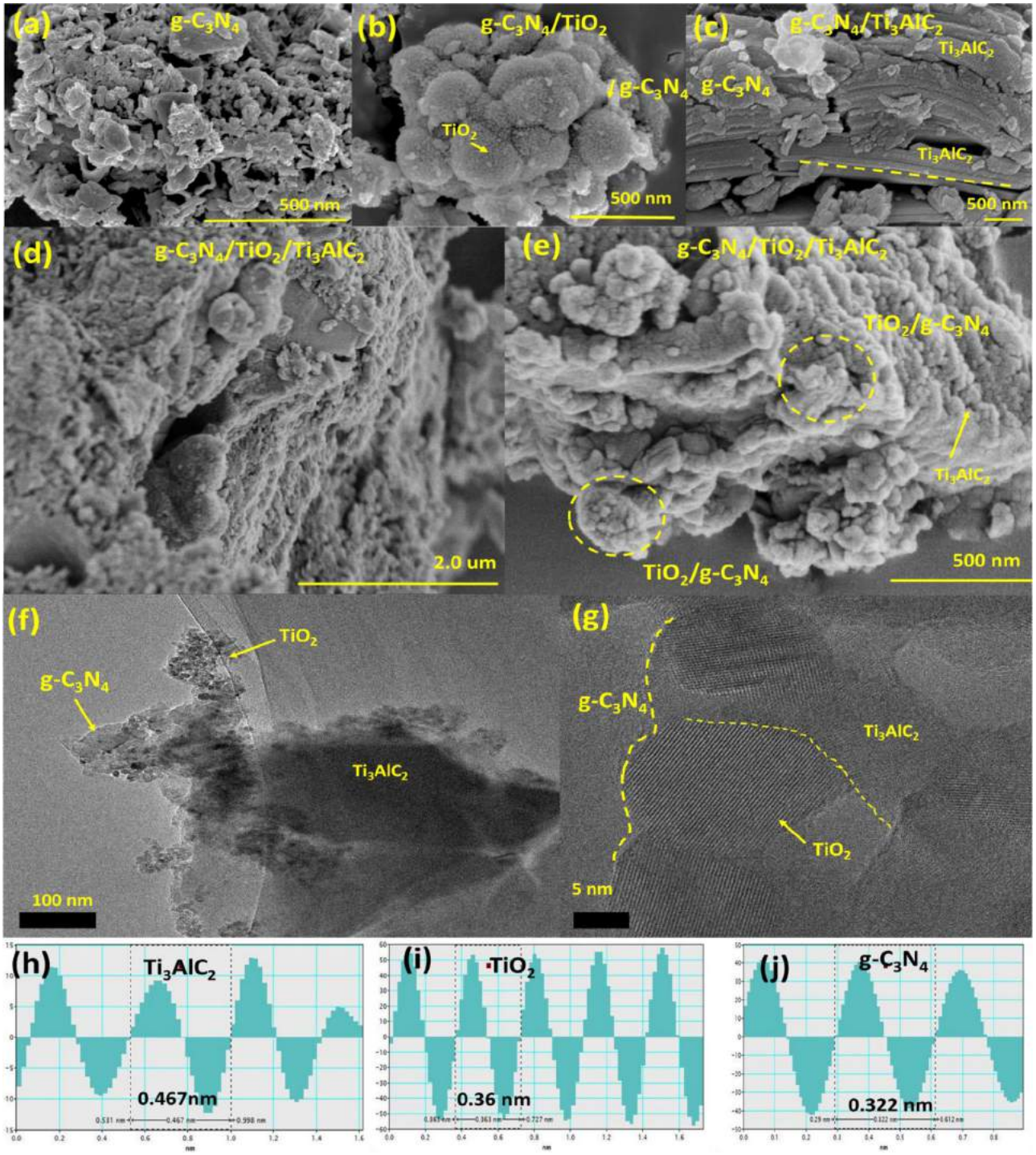

Fig. 5. (a) FESEM images of pristine g-C_3N_4, (b) g-C_3N_4/TiO_2, (c) g-C_3N_4/Ti_3AlC_2 MAX, (d, e) FESEM images of g-C_3N_4/TiO_2 NPs/Ti_3AlC_2, (f) TEM images of g-C_3N_4/TiO_2 NPs/Ti_3AlC_2, (g) HRTEM image of composite, (h-j) d-spacing of g-C_3N_4/TiO_2 NPs anchored Ti_3AlC_2 MAX composite.

that there was no obvious peak of Ti-C element in the Ti_3AlC_2 anchored TiO_2 and g-C_3N_4/TiO_2 anchored Ti_3AlC_2 composite due to lower content of Ti_3AlC_2 and lower intensity of Ti-C peak [34].

Fig. 6(b) shows XPS spectra of N 1s of g-C_3N_4, g-C_3N_4/Ti_3AlC_2 MAX and g-C_3N_4/TiO_2/Ti_3AlC_2 samples. XPS spectrum of g-C_3N_4 present three peaks with 398.78, 400.34 and 406.97 eV binding energies, corresponds to C-N=C, N-C_3 and surface modification, respectively. Similarly, g-C_3N_4/Ti_3AlC_2 MAX sample, three peaks were appeared at 398.61, 400.75 and 403.65 eV, confirming the interaction of C-N=C, N-C_3 and surface modification, respectively [40]. Finally, two peaks appeared at 399.18 and 400.75 eV belonging to C and N as C-N=C and N-C_3, respectively, in the g-C_3N_4/TiO_2 anchoredTi_3AlC_2 photocatalyst sample [15].

Fig. 6(c) shows high resolution spectra of C 1s of pristine TiO_2, 2D Ti_3AlC_2 MAX, TiO_2 NPs dispersedTi_3AlC_2, g-C_3N_4/TiO_2 loaded 2D Ti_3AlC_2 samples. All the binding energies were calibrated with adventurous carbon peak at 284.60 eV. For TiO_2, two peaks positioned at 284.60 and 288.85 eV can be ascribed to C-C and C-O bonds, respectively. Similarly, Ti_3AlC_2 sample displays three peaks with 284.60, 286.39 and 288.58 eV binding energies, be-

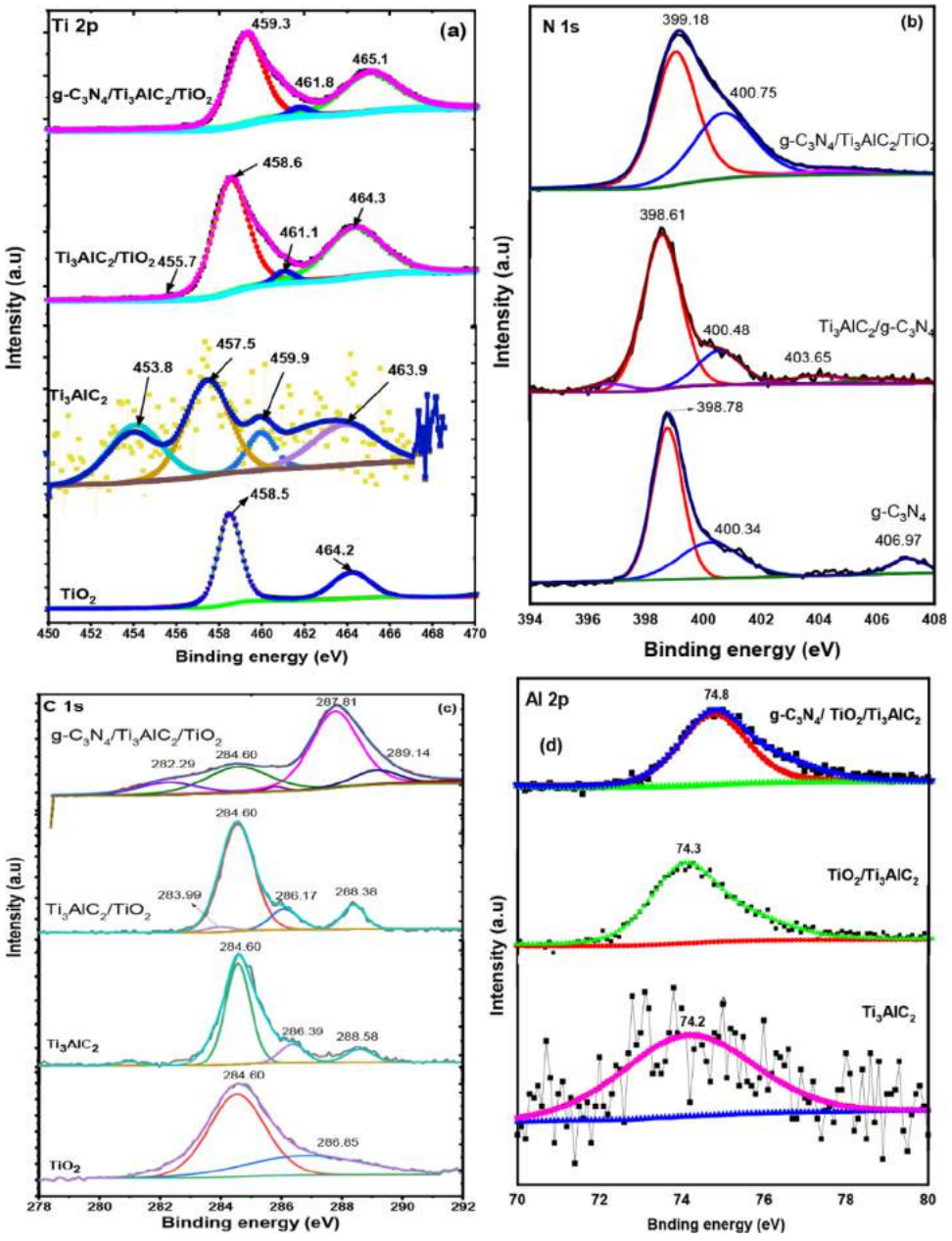

Fig. 6. XPS analysis of TiO_2, g-C_3N_4, Ti_3AlC_2 and their g-C_3N_4/TiO_2 loaded 2D Ti_3AlC_2 MAX composite samples: (a) Ti2p; (b) N 1s; (c); C 1s; (d) Al 2p.

longing to C-C, C-O and C=O bonds, respectively. The XPS plot of TiO_2 NPs/Ti_3AlC_2 displays four peaks positioned at 283.99, 284.60, 286.17 and 288.38, corresponding to Ti-C, C-C, C-O, and C=O, respectively. For the g-C_3N_4/TiO_2/Ti_3AlC_2 composite, four peaks positioned at 282.99, 284.60, 287.81 and 289.14eV can be ascribed to Ti-C, C-C, C-O and N=C-N_2, respectively. Fig. 6(d) presents XPS spectra of Al 2p for Ti_3AlC_2 MAX, Ti_3AlC_2 coupled TiO_2 and g-C_3N_4/TiO_2 dispersed Ti_3AlC_2 composite samples with binding energies 74.2, 74.3 and 74.8 eV, respectively, which confirms the present of Al in all the samples.

It could be seen that there was a positive shift in peaks of Ti, N, C and Al in the composite samples, which confirms good interaction among the component samples, which would be beneficial for efficient charges separation.

The light harvesting efficiency of TiO_2 NPs, g-C_3N_4, g-C_3N_4/TiO_2 and composite was determined by UV-visible DRS as demonstrated in Fig. 7(a). Using TiO_2, light absorption in the UV region was observed, whereas, g-C_3N_4 presents light absorption in the visible region. However, Ti_3AlC_2 did not reflect any peak in UV or the visible region, thus presents light absorption in the entire UV-visible spectrum. The g-C_3N_4 and Ti_3AlC_2 composites also shows light absorption in the visible region and similar observation could be seen in the ternary composite photocatalyst. A band gap energy of 3.14 and 2.69 eV was obtained for pristine TiO_2 and g-C_3N_4. However, when 2D Ti_3AlC_2 MAX was dispersed with TiO_2 NPs, 3.22 eV band gap energy was calculated, whereas, TiO_2/g-C_3N_4 composite shows a 3.09 eV band gap energy. When Ti_3AlC_2 was coupled with TiO_2 and g-C_3N_4, a band gap of 2.99 eV was estimated. It could be observed that the band gap energy was increased for the composite samples, probably due to introducing intra band gap states, which reflect in the absorption spectrum. In composite samples, inapplicability of Tauc plot for the calculation of band gap energy may results in an inaccurate estimation of E_g [46,47]. Previously an increased in band gap of Ru/TiO_2 was observed using Tauc plot (based on Kubelka–

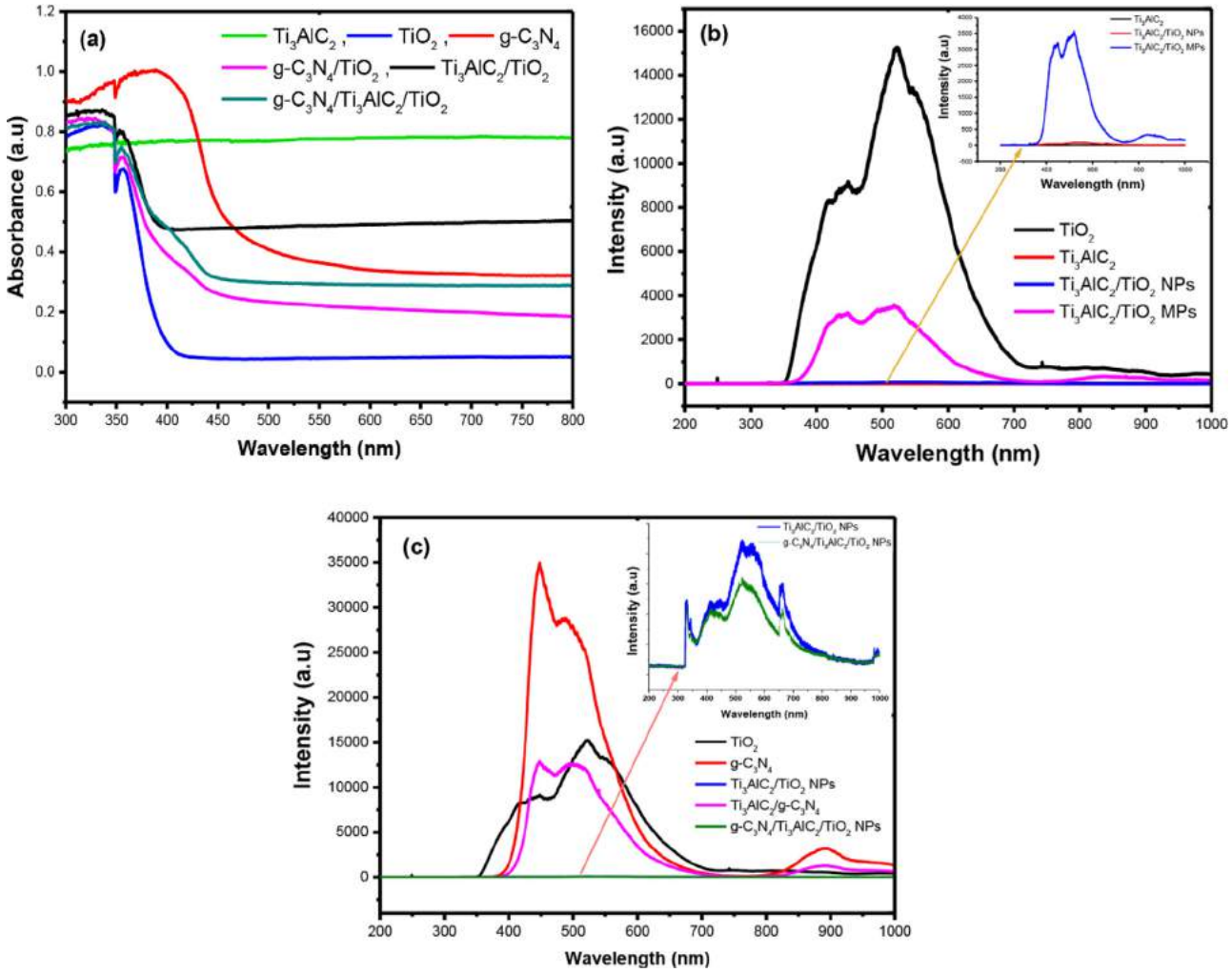

Fig. 7. (a) UV-Vis analysis of TiO_2, g-C_3N_4, Ti_3AlC_2, and Ti_3AlC_2 based composites, (b) PL spectra of TiO_2, Ti_3AlC_2 and their composite samples, (c) PL spectra of g-C_3N_4, Ti_3AlC_2 loaded TiO_2 and g-C_3N_4/TiO_2/Ti_3AlC_2 MAX composite samples.

Munk model) [48]. Similarly, an increased in band gap energy of g-C_3N_4/Bt/Ti_3C_2 heterojunction has been reported by estimating through Tauc plot method [49]. In another work, an increased in band gap of WO_3/g-C_3N_4 composite has been reported compared to pristine WO_3 and g-C_3N_4 samples [50]. All these findings show that Tauc plot can be effectively employed for calculating band gap of pure semiconductors. However, it would give inaccurate values of band gap for modified and composite samples.

The PL analysis was further performed to understand the charges separation efficiency of pristine and composite samples as shown in Fig. 7(b, c). Fig. 7(b) shows PL spectra of TiO_2 NPs, Ti_3AlC_2 and TiO_2NPs/MPs loaded Ti_3AlC_2 samples. It is obvious that highest PL intensity was observed in pristine TiO_2 due to higher charges recombination rate. A much lower PL intensity was observed when TiO_2 was loaded over 2D Ti_3AlC_2 structure, obviously, due to higher electron conductive ability of MAX phase. Comparing to TiO_2 MPs, much lower PL intensity was achieved with TiO_2 NPs anchored with Ti_3AlC_2, due to good interaction and faster electron separation.

Fig. 7(c) shows PL analysis of g-C_3N_4 and g-C_3N_4 loaded TiO_2 and Ti_3AlC_2 composite samples. Using pristine g-C_3N_4, highest PL intensity was observed, which was obviously decreased when TiO_2 was coupled with g-C_3N_4 due to their heterojunction formation. Similarly, g-C_3N_4 PL intensity was significantly reduced by coupling with Ti_3AlC_2 due to efficient charges separation through conductive MAX cocatalyst. The lowest PL intensity was achieved using g-C_3N_4/TiO_2/Ti_3AlC_2 MAX composite photocatalyst. Previously, reduced PL intensity was observed when g-C_3N_4 was coupled with Ti_3C_2 due to faster charge carrier separation [34]. In another development, reduced PL intensity in g-C_3N_4/Ti_3C_2 composite was observed due to faster charges separation [44].

3.2. Photoactivity test

The activity of various photocatalysts for CO_2 photoreduction has been evaluated under visible light irradiation. Initially, performance of Ti_3AlC_2 MAX was tested using TiO_2 NPs and MPs and the best catalyst was further combined with g-C_3N_4 to construct 2D/0D/2D heterojunction. The performance of composite catalyst was tested in a fixed bed and the monolith photoreactor under visible light irradiation. The performance of photocatalysts was quantified with the incremental production of either CO or CH_4, which were the major CO_2 reduction products. In order to verify the source of CO and CH_4 production and to confirm that the reaction is really induced by light irradiation during CO_2 photocatalysis, different sets of quality control runs were conducted using the followings: (a) using only photocatalyst under light source with inert gas, (b) Using only CO_2 and H_2O feed mixture under light flux but without loading photocatalyst. In all types of these experiments, production of either CO or CH_4 was not detected, which

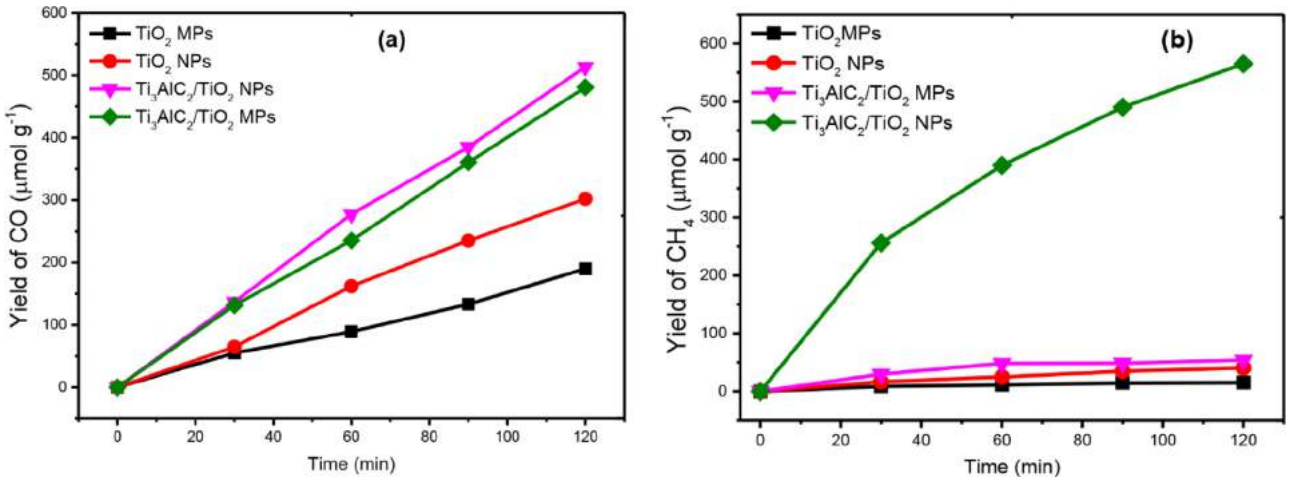

Fig. 8. Effect of different photocatalysts on photocatalytic reduction of CO_2 with H_2O to CO and CH_4 under visible light in a fixed bed photoreactor: (a) Yield of CO production, (b) Yield of CH_4 evolution.

elucidates the source of carbon originated from CO_2 during photocatalysis process.

3.2.1. Effect of TiO_2 support size

The effect of TiO_2 support size on the performance of 2D Ti_3AlC_2 MAX for photocatalytic CO_2 reduction with H_2O under UV-visible light has been demonstrated in Fig. 8. Fig. 8(a) shows the production of CO over TiO_2 NPs and TiO_2 MPs dispersed over 2D Ti_3AlC_2 multilayers. Using TiO_2 MPs, very small amount of CO was produced, which was increased by 1.585 folds higher using TiO_2 NPs. This was possibly due to faster charges separation in smaller size TiO_2 particles compared to microparticles, in which, there would be more volume recombination of charge carriers. By incorporating TiO_2 MPs with 2D Ti_3AlC_2 sheets, TiO_2 MPs efficiency was increased by 2.527 folds, indicating hindered charges recombination with their good separation through highly conductive 2D MAX material. In order to compare the performance with MPs, TiO_2 NPs were also loaded over 2D MAX structure and observed increased CO production rate with CO production efficiency of 1.70 times higher with TiO_2 NPs/Ti_3AlC_2 MAX composite, compared to pristine TiO_2 NPs, due to faster charge carrier separation. Compared with pure TiO_2 MPs, TiO_2 or TiO_2 MPs/Ti_3Al_2 MAX, the CO production rate was obviously enhanced, which is 1.06, 1.70, 2.69 folds more than employing TiO_2 MPs/Ti_3AlC_2 MAX, TiO_2 NPs and TiO_2 MPs photocatalysts, respectively. This confirms that TiO_2 NPs allows more transportation of charge carrier over the 2D MAX structure due to good dispersion and less recombing probability.

As displayed in Fig. 8(b), the continuous production of CH_4 over the entire reaction time and in the presence of pristine and modified photocatalysts was obtained. Using TiO_2 MPs, CH_4 production was very small, which was increased by 2.55 folds higher using small size TiO_2 NPs. This would probably be due to less charge's recombination in TiO_2 NPs compared to large sizes TiO_2 particles, enabling more production of methane during CO_2 photoreduction process. When TiO_2 MPs were loaded over the 2D Ti_3AlC_2 sheets, efficiency towards CH_4 production was increased by 3.57 folds. However, 10.16 folds higher photoactivity towards CH_4 production was achieved with TiO_2 NPs loaded over Ti_3AlC_2 nanosheets. This was evidently due to good interaction among the TiO_2 NPs and Ti_3AlC_2, compared to TiO_2 MPs, resulting in significantly enhanced photoactivity. All these findings confirm that TiO_2 NPs are more efficient for continuous production of CO and CH_4 during photocatalytic CO_2 reduction by H_2O in a fixed bed photoreactor.

In the current developments, different reports are available on the use of g-C_3N_4 and TiO_2 based photocatalysts materials for photocatalytic CO_2 reduction to CO and CH_4 under UV and visible light irradiations. In this regards, 2D/2D g-C_3N_4/Ti_3C_2 heterojunction composite was constructed and reported enhanced CO_2 conversion with appreciable production of CO and CH_4 [34]. Similarly, ultrathin 2D Ti_3C_2 cocatalyst with g-C_3N_4 were investigated and enhanced photocatalytic activity for CO_2 and CH_4 was identified as the main reduction products [40]. Monolithic Pd NPs loaded g-C_3N_4/reduced graphene oxide composite has been reported and found efficient CO_2 photoreduction with the production of both CO and CH_4 due to faster charge carrier separation [51]. By comparing all these findings with the current work, 2D Ti_3AlC_3 MAX dispersed TiO_2 NPs would be a promising heterojunction composite for maximizing photocatalytic activity for selective reduction of CO_2 to CO and CH_4 under visible light in a fixed bed photoreactor.

The performance of different sizes TiO_2 particles with their interaction with 2D Ti_3AlC_2 were further illustrated through schematic as demonstrated in Fig. 9. Under light irradiation, photogenerated electrons in TiO_2 MPs would be travelling a longer distance to reach the catalyst surface to takes part in CO_2 reduction process as shown in Fig. 9(a). During this travelling, they have more potential to recombine with the holes with in the surface, resulting in higher charge carrier recombination instead of being consumed during CO_2 reduction process. The lower photocatalytic activity over TiO_2 MPs would also be due to lower production of electrons and limited mass transfer rate within the internal surface, resulting in internal mass transfer limitations. Comparatively, using nanosized TiO_2 particles, they have shorter distance for the electrons to reach the external surface to react with CO_2 for its reduction as displayed in Fig. 9(b). Using TiO_2 NPs, there is less charges recombination rate compared to large sizes TiO_2, enabling higher photocatalytic performance under the same reaction conditions. More importantly, when TiO_2 MPs were attached with 2D Ti_3AlC_2 surface, they have only point contact with each other, providing less interfacial interaction for the transfer of electrons from TiO_2 MPs towards Ti_3AlC_2 surface (Fig. 9(c)). Fig. 9(d) depicts TiO_2 NPs interactions with 2D Ti_3AlC_2 surface with their good interaction, thus, providing more channels for electrons to reach the MAX surface. Comparatively, there would be more distribution of TiO_2 NPs with 2D Ti_3AlC_2 surface, thus, increasing their interaction, resulting in faster charge carrier separation with higher photocatalytic activity.

3.2.2. Effect of Ti_3AlC_2 support on heterojunction formation

The photocatalytic performance of Ti_3AlC_2 2D MAX based composite catalyst for photoinduced CO_2 conversion to CO/CH_4 under

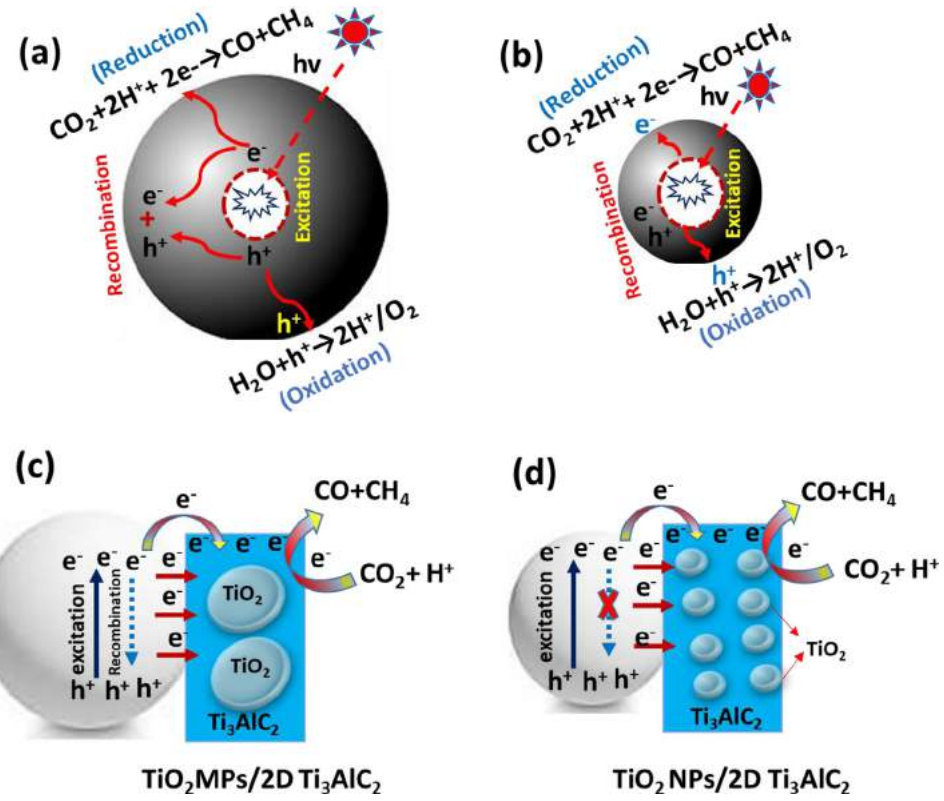

Fig. 9. Schematic of TiO_2 NPs and MPs with their interaction over Ti_3AlC_2 2D MAX structure: (a) Charges separation in TiO_2 MPs, (b) Charges separation in TiO_2 NPs, (c) Interaction of TiO_2 MPs with Ti_3AlC_2 2D MAX, (d) Interaction of 2D Ti_3AlC_2 with TiO_2 NPs.

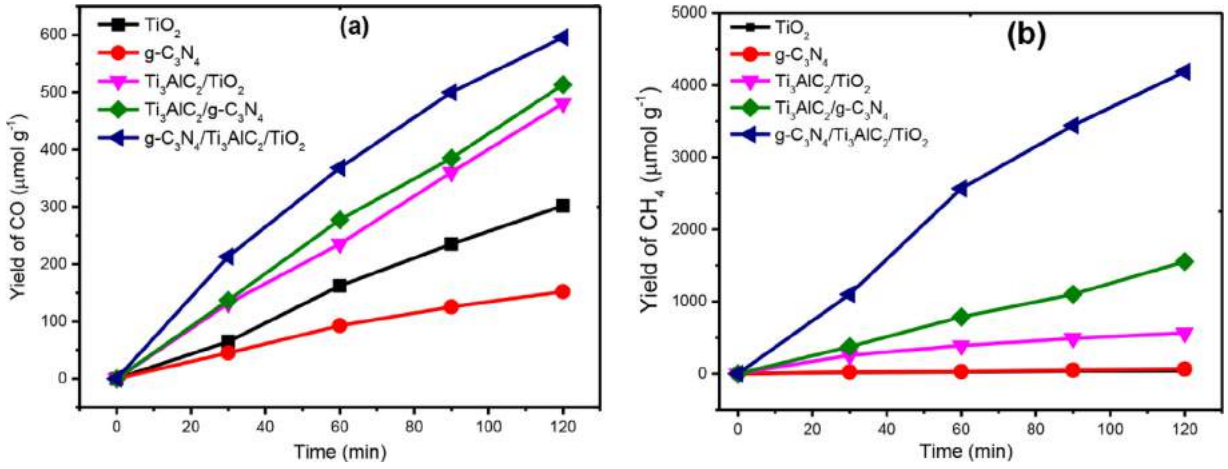

Fig. 10. Effect of 2D MAX Ti_3AlC_2 support structure on the performance of pristine TiO_2 NPs, g-C_3N_4 and their Ti_3AlC_2/TiO_2 NPs and Ti_3AlC_2/g-C_3N_4/TiO_2 NPs composite for CO and CH_4 under visible light: (a) Yield of CO production; (b) Yield of CH_4 production.

visible light is shown in Fig. 10. As shown in Fig. 10(a), CO_2 can be reduced to CO over all types of photocatalysts with time on stream. The pure TiO_2 and g-C_3N_4 photocatalysts show poor CO production, which is ascribed to faster charge carrier recombination rate in a single semiconductor. When TiO_2 NPs were dispersed over 2D MAX Ti_3AlC_2, a 1.70 folds higher photocatalytic CO production than using only pristine TiO_2, demonstrating superior charges separation by conductive 2D MAX cocatalyst. Similarly, a 3.38 folds higher CO production efficiency was observed over the 2D/2D heterojunction of g-C_3N_4 anchored Ti_3AlC_2 MAX composite, significantly higher compared to pristine g-C_3N_4, and this increment was due to hindered charges recombination rate by Ti_3AlC_2 cocatalyst. The CO evolution reached highest over g-$C_3N_4/TiO_2/Ti_3AlC_2$ MAX composite, which is about 1.16, 1.23, 1.97 and 3.93 times more than applying g-C_3N_4/Ti_3AlC_2 MAX, TiO_2 NPs/Ti_3AlC_2, TiO_2 and g-C_3N_4 samples, respectively. This promotion affirms that reduction efficiency was greatly promoted by 2D MAX Ti_3AlC_2 mediator as co-catalyst to trap and transport electrons during CO_2 photoreduction process over g-C_3N_4/TiO_2 2D/0D composite under visible light. The enhanced photocatalytic CO_2 reduction to CO and CH_4 has been reported over 2D/2D Ti_3C_2/g-C_3N_4 heterojunction due to spatial charge carriers separation in the presence of conductive Ti_3C_3 as cocatalyst [34].

The further investigation of pure and composite photocatalysts were explored towards CO_2 reduction to CH_4 as shown Fig. 10(b). Similar to photocatalytic CO production, during CO_2 reduction pro-

cess over pristine TiO_2 and g-C_3N_4, poor photocatalytic activity with very small amount of CH_4 was attained, which was also much lower than CO production. This was evidently due to faster charges recombination rate, and the availability of electrons was not enough to generate CH_4 molecules. However, when Ti_3AlC_2 was attached to TiO_2 NPs and g-C_3N_4, a CH_4 production of 13.11 and 27.99 folds higher was produced than using TiO_2 and g-C_3N_4 samples, respectively. Highest CH_4 evolution was observed when 2D Ti_3AlC_2 was attached to g-C_3N_4/TiO_2 heterojunction, which is 2.73, 7.45, 46.40 and 97.71 times more than employing g-C_3N_4/Ti_3AlC_2 MAX, TiO_2 NPs/Ti_3AlC_2 MAX, pristine g-C_3N_4 and TiO_2 photocatalysts, respectively. This confirms that composite photocatalyst is very promising pertaining to efficient CO_2 reduction to CH_4. This affirms that 2D MAX is a promising cocatalyst and mediator in stimulating photocatalytic CO_2 methanation under visible light.

Previously, several reports present photocatalytic CO_2 reduction to CO and CH_4 over various types of semiconductors photocatalysts. Enhanced production of CO/CH_4 during photocatalytic reduction of CO_2 over TiO_2-Cu_2ZnSnS_4 hybrid heterojunction has been reported [43]. In another work, porous 3D Cu-doped g-C_3N_4 was synthesized for the conversion of CO_2 to CO as the major product [52]. Using visible light, CO_2 reduction to CH_4 plasmonic Au-Pd modified TiO_2 has been reported [7]. We reported dynamic production of CH_4 during CO_2 conversion by H_2 over Mt/g-C_3N_4 composite [53]. Recently, 2D ultrathin Ti_3C_2 MXene anchored on porous g-C_3N_4 as a cocatalyst has been investigated for CO_2 to CH_4 reduction under visible-light [40]. All these results and developments further confirm good photoactivity and productivity during CO_2 photocatalysis with CH_4 production in a single step CO_2 photoreduction process, however, methane formation efficiency is entirely dependent on the use of cocatalyst or heterojunction formation for efficient charge carrier separation. In the current work, 2D MAX Ti_3AlC_2 found very promising for trapping and transporting photogenerated electrons towards CO_2 for its activation for CH_4 production.

3.3. Performance analysis of monolith and fixed bed photoreactors

In order to further explore the photocatalytic performance of g-C_3N_4/TiO_2/Ti_3AlC_2, it was investigated in different photocatalytic systems. It is well established that activity of photocatalyst is greatly dependent on light intensity which is directly related with the production of electrons. Besides, geometry and design of photoreactors also promote to maximize photon flux distribution, enabling to provide active surface area with efficient mass transfer rate and minimum light diffusion effects. The photocatalytic activity of g-C_3N_4/TiO_2/Ti_3AlC_2 2D MAX composite under light intensity of 20 and 100 mW cm^{-2} was further elucidated using monolith and fixed bed photoreactor and the results are depicted in Fig. 11. As shown in Fig. 11(a), different evolution rate of CH_4 was detected by varying light intensity in a fixed-bed photoreactor. Evidently, production of CH_4 was continuous over the irradiation time, while employing different light intensities. Using fixed bed reactor with light intensity 20 mW cm^{-2}, CH_4 production was not efficient due to less light intensity being consumed for the production of electrons. However, 3.587 folds higher CH_4 production was obtained under 100 mW cm^{-2} light intensity in a fixed bed reactor, while keeping operating conditions constant. This was evidently due to more production of electrons and their efficient utilization for the conversion of CO_2 to CH_4. Comparatively, performance of monolith photoreactor was not efficient for CH_4 production and CH_4 production was declined by 53.99 folds than it was produced in a fixed bed reactor under 100 mW cm^{-2} light intensity. The less electrons production in a monolith photoreactor under visible light irradiation was probably due to lower penetration power of visible light inside microchannels.

Fig. 11(b) shows the production of CO during photocatalytic CO_2 reduction with different light intensities in a monolith and fixed bed photoreactor. Using lower power lamp (20 mW cm^{-2}), the yield rate of CO was not much efficient, but it was increased by 1.924 folds when 100 mW cm^{-2} light intensity was employed through fixed-bed photoreactor. A 2.64 folds increased in evolution rate of CO was obtained through monolith photoreactor compared with fixed bed photoreactor. These findings revel that monolith can promote CO production, whereas, fixed bed photoreactor was favorable for methane formation.

The performance of fixed bed and monolith photoreactor is further compared with the similar work reported in the literature. Previously, we investigated the performance of fixed bed and monolith photoreactor for photocatalytic CO_2 reduction under UV-light irradiation. It was observed that the performance of Ni and MMT modified TiO_2 was obviously increased using monolith photoreactor compared to fixed bed. This was due to higher penetration of UV-light inside the monolith channels, enabling larger illuminated volume for CO_2 reduction process and main products observed were CO and H_2 [54]. Similarly, performance of fixed bed and monolith photoreactor was investigated for photocatalytic CO_2 reduction over Ag-La/g-C_3N_4 composite under UV and visible light irradiation. Higher efficiency of fixed bed reactor under visible light irradiation was observed, while monolith photoreactor found more efficient under UV-light irradiation [41]. Liou et al., investigated the performance of monolith photoreactor under visible light irradiation. Lower CO_2 reduction efficiency of monolith was observed using NiO/$InTaO_4$ composite photocatalyst under visible light irradiation. This was due to less penetration power of visible light inside the microchannels. However, monolith performance was significantly enhanced using PMMA optical fibers to increase illumination inside the channels. All these findings confirm that monolith photoreactor is less efficient compared to fixed bed photoreactor under visible light irradiation due to less penetration power of visible light.

Comparatively, performance of monolith was lower compared to fixed bed photoreactor and this declined in photocatalytic activity was further illustrated based on light penetration limitations and mass transfer affects as depicted in Fig. 12. The schematic illustration of photocatalytic CO_2 reduction with H_2O in a fixed bed photoreactor has been demonstrated in Fig. 12(a). Obviously, using fixed bed photoreactor, catalyst is uniformly distributed at the reactor surface, in which, only top surface of catalyst would be available for photocatalytic CO_2 reduction process. In this case, all the light irradiations and reactants have potential to be absorbed over the photocatalyst surface under light irradiation. Thus, photocatalytic CO_2 reduction process with proficient evolution rate of CO/CH_4 during photo-induced CO_2 reduction process. By increasing light intensity 20 to 100 mW cm^{-2}, methane evolution was further improved due to higher photon flux strikes at the catalyst surface, enabling efficient CO_2 conversion to CH_4 due to more production of electrons.

The schematic illustration for the conversion of CO_2 with H_2O in a monolith photoreactor has been depicted in Fig. 12(b). Compared to fixed bed reactor, monolithic support has multiple channels loaded with thin film of photocatalyst. The reaction occurs over the catalyst surface in all the channels which has larger exposed surface area for the adsorption of reactants. As the visible light has been used in this work, thus, penetration power of light inside the microchannels was not efficient and most of the light was reflected back from the top surface of the monolith. Due to less penetration power of light inside the channels, it has less interaction with the catalyst and only the reactants attached over the photocatalyst surface without photocatalysis process. Thus, lower

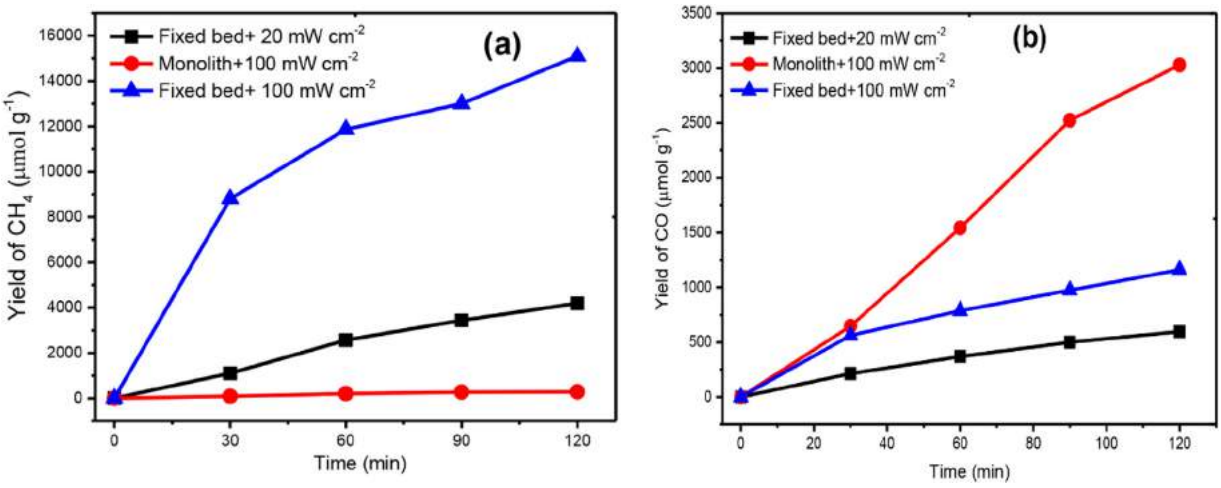

Fig. 11. Performance analysis of fixed bed and monolith photoreactor under visible light of different light intensities (20 and 100 mW cm^{-2}) for the production CO/ CH_4; (a) CH_4 evolution; (b) CO evolution.

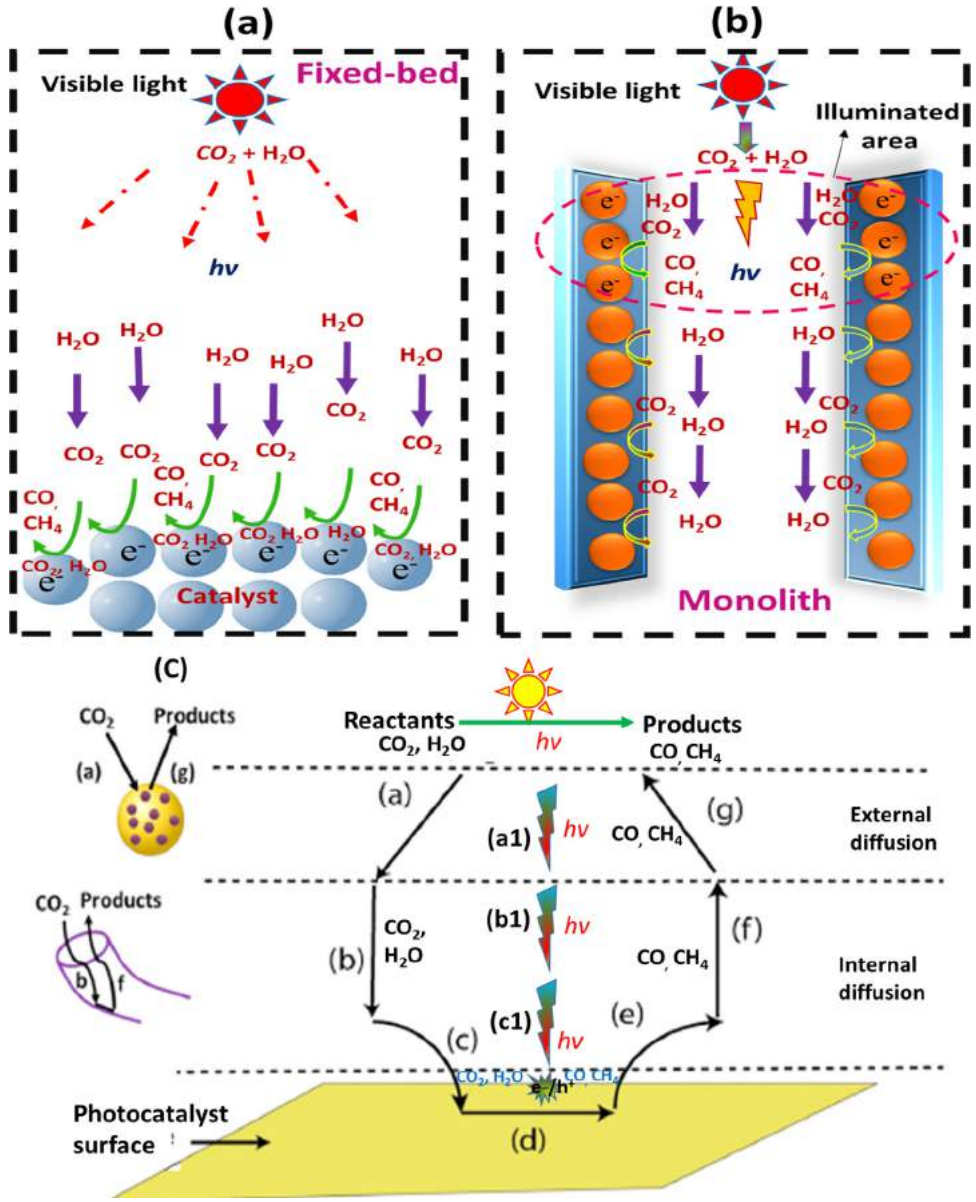

Fig. 12. Schematic illustration for photocatalytic CO_2 reduction process in a fixed bed and monolith photoreactor: (a) Fixed bed photoreactor, (b) Monolith photoreactor, (c) Mass transfer process with external and internal diffusion affects.

Table 1
Evaluation of production rate, selectivity, QY and TON for CO and CH_4 production over g-C_3N_4 and modified g-C_3N_4 samples.

Photocatalyst	Intensity (mW cm^{-2})	Photoreactor	Production rate (μmole g^{-1} h^{-1})		Selectivity (%)		QY (%)	
			CO	CH_4	CO	CH_4	CO	CH_4
TiO_2 MPs	20	Fixed-bed	94.61	7.78	75.25	24.75	0.401	0.132
TiO_2 NPs	20	Fixed-bed	150.71	21.53	63.64	36.36	0.638	0.365
g-C_3N_4	20	Fixed-bed	75.64	27.54	40.71	59.29	0.320	0.467
TiO_2MPs/Ti_3AlC_2	20	Fixed-bed	240.32	27.025	68.97	31.03	0.339	0.153
TiO_2 NPs/Ti_3AlC_2	20	Fixed-bed	240.09	282.39	17.53	82.47	1.695	7.975
g-C_3N_4/Ti_3AlC_2 MAX	20	Fixed-bed	255.81	770.74	7.66	92.34	1.084	13.059
g-C_3N_4/TiO_2/Ti_3AlC_2 MAX	20	Fixed-bed	297.26	2103.50	3.41	96.59	1.259	35.642
g-C_3N_4/TiO_2/Ti_3AlC_2 MAX	100	Fixed-bed	571.99	7546.83	1.86	98.14	0.485	25.575
g-C_3N_4/TiO_2/Ti_3AlC_2 MAX	100	Monolith	1510.44	139.77	72.99	27.01	2.133	0.789

photocatalytic CO_2 reduction efficiency was achieved using monolith photoreactor.

The possible performance mechanism in a monolith and fixed bed photoreactor can be further demonstrated based on mass transfer process and light diffusion process as shown in Fig. 12(c). In heterogenous photocatalysts, reactants have to reach the catalyst surface through external and internal boundaries, which limits mass transfer process. In a fixed bed photoreactor, a major challenge is the transfer of reactants to reach the catalyst surface and also lower adsorption-desorption process. Comparatively, monolithic support has no external or internal mass transfer limitations due to catalyst loaded over the channels surface as a thin film. However, photocatalytic activity in a fixed bed photoreactor was higher due to efficient light distribution over the catalyst surface compared to using monolithic support with microchannels. This shows newly fabricated structured photocatalyst and photoreactor performance is greatly dependent on the interaction of three components i.e., reactants, catalyst and light. If any process is not efficient, the photocatalytic activity would be declined.

The CO and CH_4 production rate, selectivity and quantum yield over different types of photocatalysts in a fixed bed and monolith photoreactor are further summarized in a Table 1. Using TiO_2 MPs, 97.61 and 7.78 μmole g^{-1} h^{-1} of CO and CH_4 yield rates, respectively, were produced and increased to 150.71 and 21.53 μmole g^{-1} h^{-1} for CO and CH_4 production with TiO_2 NPs. Similarly, pristine g-C_3N_4 producing CO and CH_4 of 75.64 and 27.54 μmole g^{-1} h^{-1} under visible light while using fixed bed photoreactor. The CO and CH_4 yield rates were increased to 240.09 and 282.39 μmole g^{-1} h^{-1}, respectively, when TiO_2 NPs were dispersed over the 2D Ti_3AlC_2 multilayers, which was much higher than using TiO_2 MPs attached to 2D MAX structure. This was evidently due to superior separation of charges in the presence of conductive characteristics of MAX structure. As the TiO_2 MPs were well-dispersed with MAX structure, thus, proficient separation of charge carrier was achieved. Using g-C_3N_4/Ti_3AlC_2 MAX 2D/2D heterojunction, yield rate of CO and CH_4 of 255.81 and 770.74 μmole g^{-1} h^{-1}, respectively, which confirms g-C_3N_4 is favorable to promote CH_4 production compared to TiO_2 NPs with selectivity 7.66% and 92.34% for CO and CH_4, respectively. The highest CO and CH_4 production of 297.26 and 2103.50 μmole g^{-1} h^{-1} achieved comparing to over g-C_3N_4/TiO_2/Ti_3AlC_2 MAX at selectivity 3.41% and 69.58%, in a fixed bed photoreactor, by employing 20 mW cm^{-2} light intensity.

Furthermore, by increasing light intensity to 100 mW cm^{-2}, CO and CH_4 yield rate of 571.99 and 7546.83 μmole g^{-1} h^{-1}, respectively at selectivity 1.86% and 98.14% were achieved. This confirms that light intensity is favorable to promote both photoactivity and selectivity, while employing fixed-bed photocatalytic reactor system. In the case of photocatalytic activity of composite photocatalyst in a monolith reactor with 100 mW cm^{-2}, CO and CH_4 yield rate of 1510.44 and 139.77 μmole g^{-1} h^{-1} at selectivity 72.99% and 2.133%, respectively, were obtained. This reveals that monolith photoreactor is less selective for methane formation by comparing with fixed bed photoreactor due to higher utilization of photon flux compared to monolith photoreactor.

The quantum yield (QY) was further calculated to elucidate the CO and CH_4 production performance in a monolith and fixed bed photoreactor and their results are summarized in Table 1. It is obvious that g-C_3N_4/TiO_2/Ti_3AlC_2 composite catalyst gave highest QY due to more utilization of higher photon flux through using fixed bed photoreactor during photoinduced CO_2 reduction to CH_4. A QY of 35.642% for CH_4 attained using g-C_3N_4/TiO_2/Ti_3AlC_2 MAX composite at intensity 20 mW cm^{-2} in a fixed bed photocatalytic reactor, which is 2.73, 4.47 and 232.95 folds higher than using g-C_3N_4/Ti_3AlC_2 MAX, TiO_2 NPs/Ti_3AlC_2 and TiO_2 MPs/Ti_3AlC_2 composite samples, respectively. By increasing photon flux from 20 to 100 mW cm^{-2}, a QY of 25.575% for CH_4 production was calculated, which is 1.394 folds lower than using lower power lamp in a fixed bed photoreactor. This reveals that all the photon flux strikes over the catalyst surface was not fully utilized for the production of charge carrier. This further confirms that fixed bed photoreactor become less efficient with increasing photon flux due to the availability of external surface of photocatalyst for photocatalytic reaction.

Furthermore, a QY of 2.133% and 0.789% was achieved in a monolith photoreactor for the production of CO and CH_4 under light intensity 100 mW cm^{-2}. This QY for CO production was 4.39 folds higher and 32.41 folds lower for CH_4 by comparing photocatalytic activity in a fixed bed photoreactor under the same operating condition. All above discussion further confirm that fixed bed photoreactor is proficient under visible light irradiation compared to monolith photoreactor for photocatalytic CO_2 reduction.

3.4. Proposed mechanism for CO_2 photoreduction

During photoinduced CO_2 reduction by H_2O, it involves the utilization of electrons and holes photoinduced over the composite photocatalyst surface for CO and CH_4 production. The band structure of TiO_2 and g-C_3N_4 were estimated to understand the reaction mechanism. As discussed previously, band gap energies of 3.14 eV and 2.69 eV were estimated for TiO_2 and g-C_3N_4 samples, based on their UV-visible spectra, respectively. Similarly, based on XPS wide spectra, valance band (VB) positions of +1.46 and +2.63 eV were estimated for g-C_3N_4 and TiO_2, respectively. Giving this analysis, conduction band (CB) values for g-C_3N_4 and TiO_2 of -1.23 eV and -0.52 eV, respectively, were obtained. According to experimental results, photoactivity of pristine TiO_2 was much higher compared to pristine g-C_3N_4, which reveals that oxidation potential of g-C_3N_4 is not strong enough to efficiently oxidize water. More importantly, in the presence of TiO_2 and g-C_3N_4 with MAX as the cocatalyst, a significantly enhanced photocatalytic activity was achieved. This significantly improved CO_2 reduction to CO and CH_4 reveals that the charge separation between both the semiconductors did

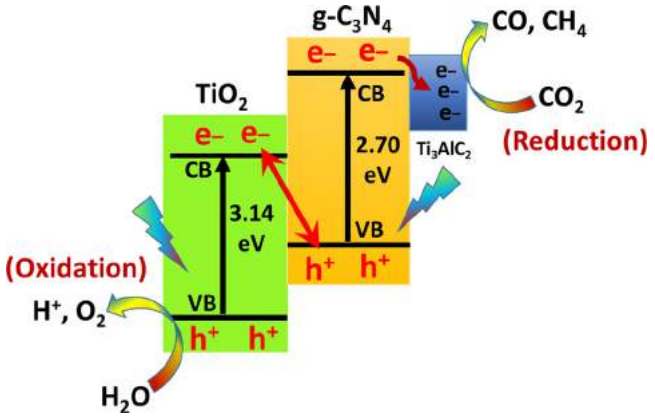

Fig. 13. Schematic illustration of S-scheme heterojunction for photocatalytic CO_2 reduction with H_2O over 2D MAX Ti_3AlC_2 dispersed g-C_3N_4/TiO_2 composite.

not comply with type II heterojunction. Recently, He and coworkers reported that TiO_2 has strong oxidation potential compared to g-C_3N_4, whereas, VB of g-C_3N_4 could not directly oxidize water into hydroxyl ions. The S-scheme mechanism has been proposed in their work to explain photocatalytic CO_2 reduction efficiency of TiO_2 and g-C_3N_4 with TiC as the cocatalyst to trap the electrons [55]. In another work, S-scheme heterojunction for photocatalytic hydrogen production over 2D/2D WO_3/g-CN_4 has been reported [56]. Similarly, S-scheme heterojunction of Bi_2O_3/TiO_2 with higher photocatalytic activity has been reported [57].

Therefore, in the current study, when TiO_2 is coupled with g-C_3N_4 and MAX, a significantly enhanced CO_2 reduction with higher CO/CH_4 evolution was observed due to S-scheme charge transfer mechanism and similarly reported in the literature [58]. A schematic presentation of possible photocatalytic CO_2 reduction with H_2O through S-scheme heterojunction mechanism has been demonstrated in Fig. 13. As the fermi level of g-C_3N_4 is higher than the fermi level of TiO_2, and this difference derives the charge transfer from g-C_3N_4 to TiO_2 until their Fermi level reached to equilibrium. At equilibrium, at the interface of both the semiconductors, an internal electric field, could be formed, which favored the transfer and separation of charges. The internal electric field minimized their recombination [55,59]. The presence of conductive Ti_3AlC_2 MAX further promoted the separation of electrons. Thus, useful electrons in the CB of g-C_3N_4 were prone to migrating to conductive TiAlC for the multielectron reduction process of CO_2. Similarly, useful holes in the VB of TiO_2 are preserved for the oxidation of water. Recently, Au loaded 2D/2D Bi_2MoO_6/g-C_3N_4 S-scheme heterojunction has been proposed in which significant enhanced charges separation has been reported due to interface field with Au as cocatalyst to trap electrons [60]. In another work, significantly enhanced photocatalytic hydrogen production has been reported over WO_3/TiO_2/GO step-scheme heterojunction. The enhanced photoactivity was proposed due to S-scheme heterojunction formation between WO_3/TiO_2 and efficient electron separation from TiO_2 to GO [61].

In summary, powerful photogenerated electron and holes are in the CB of g-C_3N_4 and VB of TiO_2 participated in different photocatalytic reactions The electrons photogenerated during photocatalysis are consumed by CO_2 for its reduction, whereas, holes are consumed during water oxidation process as illustrated in Eqs. (6) and (7). Finally, CO and CH_4 were produced by consuming 2 and 8 electrons as presented in Eqs. (8) and (9), respectively.

$$CO_2 + e^- \rightarrow \bullet CO_2^- \quad (6)$$

$$H_2O + 2h^+ \rightarrow \frac{1}{2}O_2 + 2H^+ (1.23 \text{ eV vs NHE}) \quad (7)$$

$$CO_2 + 2H^+ + 2e^- \rightarrow CO + H_2O (-0.48 \text{ eV vs NHE}) \quad (8)$$

$$CO_2 + 8H^+ + 8e^- \rightarrow CH_4 + 2H_2O (-0.24 \text{ eV vs NHE}) \quad (9)$$

According to thermodynamics, photocatalytic CO_2 reduction to CO/CH_4 depends on the conduction bands of semiconductors and products reduction potential. The conduction band of TiO_2 (-0.52 eV) is obviously more negative than CO (-0.48 eV) and CH_4 (-0.24 eV) reduction potential, which is enough to drive this reduction reaction. Similarly, VB of g-C_3N_4 (+1.46 eV) is more positive than the oxidation potential of O_2 (+1.23 eV vs NHE) during water oxidation process [34]. As discussed previously, CH_4 production over 2D MAX dispersed g-C_3N_4/TiO_2 composite was much higher compared to CO evolution rate. As 2 electrons are required for CO formation compared to 8 electrons consumed during the formation of CH_4. Thus, the main reason for improved photocatalytic activity towards CH_4 formation would be due to more production and separation of electrons over g-C_3N_4 and TiO_2 S-scheme heterojunction with efficient electrons separation by 2D MAX Ti_3AlC_2 structure. Therefore, well designed 2D MAX Ti_3AlC_2 dispersed g-C_3N_4/TiO_2 can be used as an efficient composite catalyst for selective production of fuels through photocatalytic CO_2 methanation under visible light irradiation.

4. Conclusions

In conclusion, 2D MAX dispersed g-C_3N_4/TiO_2 composite was successfully developed and tested for photocatalytic CO_2 reduction under visible light. The main products identified were CO and CH_4, whereas, their selectivity was greatly affected by using different sizes TiO_2 particles and constructing 2D MAX based composites. Using TiO_2 MPs, lower CO_2 reduction efficiency was observed, which was obviously increased through employing TiO_2 NPs. The highest CO and CH_4 production g-C_3N_4/TiO_2/Ti_3AlC_2 MAX of 297.26 and 2103.50 μmole g^{-1} h^{-1} were achieved at selectivity 3.41% and 69.58%, respectively in a fixed bed photoreactor with 20 mW cm^{-2} light intensity. More importantly, when light intensity was increased by 5 folds, CH_4 production rate was increased by 3.59 folds under visible light. The performance of composite catalyst was further investigated in a fixed bed and monolith photoreactor. It was noticed that monolithic support increased CO production by 2.64 folds, whereas, 53.99 times lower CH_4 production was obtained as comparing with fixed bed photoreactor. Using monolith microchannel photoreactor, QY for CO production was 4.39 folds higher and 32.41 folds lower for CH_4 production than using fixed bed photoreactor. The lower performance of a monolith photoreactor was due to less visible light penetration into the microchannels. Therefore, well designed 2D MAX Ti_3AlC_2 dispersed g-C_3N_4/TiO_2 can be used as an efficient structured composite photocatalyst for selective photocatalytic CO_2 methanation under visible light in a fixed bed photoreactor.

Acknowledgement

The authors would like to extend their deepest appreciation to Ministry of Higher Education (MOHE), Malaysia, for financial support of this work under Fundamental Research Grant Scheme (No. R.J130000.7851.5F384).

Supplementary materials

Supplementary material associated with this article can be found, in the online version, at doi:10.1016/j.jmst.2021.08.019.

References

[1] Y. Xia, B. Cheng, J. Fan, J. Yu, G. Liu, Sci. China Mater. 63 (2020) 552–565.
[2] Y. Wang, J. Liu, Y. Wang, M. Zhang, RSC Adv. 10 (2020) 8821–8824.
[3] A. Bafaqeer, M. Tahir, A.A. Khan, N.A.S. Amin, Ind. Eng. Chem. Res. 58 (2019) 8612–8624.
[4] F.Y. Xu, K. Meng, B.C. Zhu, H.B. Liu, J.S. Xu, J.G. Yu, Adv. Funct. Mater. 29 (2019) 1904256.
[5] M. Liu, L. Zheng, X. Bao, Z. Wang, P. Wang, Y. Liu, H. Cheng, Y. Dai, B. Huang, Z. Zheng, Chem. Eng. J. 405 (2021) 126654.
[6] N.T. Thanh Truc, L. Giang Bach, N. Thi Hanh, T.D. Pham, N. Thi Phuong Le Chi, D.T. Tran, M.V. Nguyen, V.N. Nguyen, J. Colloid Interface Sci. 540 (2019) 1–8.
[7] A. Ziarati, A. Badiei, R. Luque, M. Dadras, T. Burgi, ACS Sustainable Chem. Eng. 8 (2020) 3689–3696.
[8] S. Zhu, W. Liao, M. Zhang, S. Liang, Chem. Eng. J. 361 (2019) 461–469.
[9] O. Mekasuwandumrong, N. Jantarasorn, J. Panpranot, M. Ratova, P. Kelly, P. Praserthdam, Ceram. Int. 45 (2019) 22961–22971.
[10] J. Jin, S. Chen, J. Wang, C. Chen, T. Peng, Appl. Catal. B 263 (2020) 118353.
[11] A. Larimi, M. Rahimi, F. Khorasheh, Renew. Energy 145 (2020) 1862–1869.
[12] A. Raza, H. Shen, A.A. Haidry, L. Sun, R. Liu, S. Cui, J. CO_2 Util 37 (2020) 260–271.
[13] Z. Wang, Y. Chen, L. Zhang, B. Cheng, J. Yu, J. Fan, J. Mater. Sci. Technol. 56 (2020) 143–150.
[14] M. Suleman Tahir, N. Manzoor, M. Sagir, M.B. Tahir, T. Nawaz, Fuel 285 (2021) 119206.
[15] J.M. Li, L. Zhao, S.M. Wang, J. Li, G.H. Wang, J. Wang, Appl. Surf. Sci. 515 (2020) 145922.
[16] Y. Li, M. Zhou, B. Cheng, Y. Shao, J. Mater. Sci. Technol. 56 (2020) 1–17.
[17] C. Wang, X. Liu, W. He, Y. Zhao, Y. Wei, J. Xiong, J. Liu, J. Li, W. Song, X. Zhang, Z. Zhao, J. Catal. 389 (2020) 440–449.
[18] X. Li, J. Yu, M. Jaroniec, X. Chen, Chem Rev 119 (2019) 3962–4179.
[19] Y. Gao, F. Chen, Z. Chen, H. Shi, J. Mater. Sci. Technol. 56 (2020) 227–235.
[20] M.-M. Fang, J.-X. Shao, X.-G. Huang, J.-Y. Wang, W. Chen, J. Mater. Sci. Technol. 56 (2020) 133–142.
[21] X. Zhang, K. Hu, X. Zhang, W. Ali, Z. Li, Y. Qu, H. Wang, Q. Zhang, L. Jing, Appl. Surf. Sci. 492 (2019) 125–134.
[22] A. Muhammad, M. Tahir, S.S.A. Al-Shahrani, A. Mahmood Ali, S.-u. Rather, Appl. Surf. Sci. 504 (2019) 144177.
[23] M. Tahir, B. Tahir, M.G.M. Nawawi, M. Hussain, A. Muhammad, Appl. Surf. Sci. 485 (2019) 450–461.
[24] H. Guo, M. Chen, Q. Zhong, Y. Wang, W. Ma, J. Ding, J. CO_2 Util 33 (2019) 233–241.
[25] A. Bafaqeer, M. Tahir, N.A.S. Amin, Appl. Catal. B 242 (2019) 312–326.
[26] C. Wang, Y. Zhao, H. Xu, Y. Li, Y. Wei, J. Liu, Z. Zhao, Appl. Catal. B 263 (2020) 118314.
[27] P. Ganguly, M. Harb, Z. Cao, L. Cavallo, A. Breen, S. Dervin, D.D. Dionysiou, S.C. Pillai, ACS Energy Lett 4 (2019) 1687–1709.
[28] K. Li, S. Zhang, Y. Li, J. Fan, K. Lv, Chin. J. Catal. 42 (2021) 3–14.
[29] C. Torres, R. Quispe, N.Z. Calderón, L. Eggert, M. Hopfeld, C. Rojas, M.K. Camargo, A. Bund, P. Schaaf, R. Grieseler, Appl. Surf. Sci. 537 (2021) 147864.
[30] L. Cheng, X. Li, H. Zhang, Q. Xiang, J. Phys. Chem. Lett. 10 (2019) 3488–3494.
[31] L.F. Hong, R.T. Guo, Y. Yuan, X.Y. Ji, Z.S. Li, Z.D. Lin, W.G. Pan, Mater. Today Energy 18 (2020) 100521.
[32] B. Tahir, P.W. Er, M. Tahir, M.G.M. Nawawi, M. Siraj, H. Alias, A. Fatehmulla, J. Environ. Chem. Eng. 8 (2020) 104529.
[33] Y. Wang, Y. Zhou, M. Han, Y. Xi, H. You, X. Hao, Z. Li, J. Zhou, D. Song, D. Wang, F. Gao, Small 15 (2019) 1–8.
[34] C. Yang, Q. Tan, Q. Li, J. Zhou, J. Fan, B. Li, J. Sun, K. Lv, Appl. Catal. B 268 (2020) 118738.
[35] S. Cao, B. Shen, T. Tong, J. Fu, J. Yu, Adv. Funct. Mater. 28 (2018) 800136.
[36] K. Wang, H. Du, Z. Wang, M. Gao, H. Pan, Y. Liu, Int. J. Hydrog. Energy 42 (2017) 4244–4251.
[37] S. Tasleem, M. Tahir, Z.Y. Zakaria, J. Alloys Compd. 842 (2020) 155752.
[38] Y. Zhuang, Y. Liu, X. Meng, Appl. Surf. Sci. 496 (2019) 143647.
[39] J. Low, L. Zhang, T. Tong, B. Shen, J. Yu, J. Catal. 361 (2018) 255–266.
[40] J. Hu, J. Ding, Q. Zhong, J. Colloid Interface Sci. 582 (Pt B) (2020) 647–657.
[41] B. Tahir, M. Tahir, N.A.S. Amin, Appl. Catal. B 248 (2019) 167–183.
[42] M. Tahir, J. CO_2 Util 37 (2020) 134–146.
[43] A. Raza, H. Shen, A.A. Haidry, M.K. Shahzad, L. Sun, Appl. Surf. Sci. 529 (2020) 147005.
[44] Q. Tang, Z. Sun, S. Deng, H. Wang, Z. Wu, J. Colloid Interface Sci. 564 (2020) 406–417.
[45] H. Shi, J. Du, J. Hou, W. Ni, C. Song, K. Li, G.G. Gurzadyan, X. Guo, J. CO_2 Util 38 (2020) 16–23.
[46] P. Makula, M. Pacia, W. Macyk, J. Phys. Chem. Lett. 9 (2018) 6814–6817.
[47] B. Ohtani, J. Photochem. Photobiol. C 11 (2010) 157–178.
[48] P. Apopei, C. Catrinescu, C. Teodosiu, S. Royer, Appl. Catal. B 160-161 (2014) 374–382.
[49] M. Tahir, B. Tahir, Chem. Eng. J. 400 (2020) 125868.
[50] B. Tahir, M. Tahir, M.G.M. Nawawi, J. CO_2 Util 41 (2020) 101270.
[51] R. Zhang, Z. Huang, C. Li, Y. Zuo, Y. Zhou, Appl. Surf. Sci. 475 (2019) 953–960.
[52] Z. Sun, W. Fang, L. Zhao, H. Wang, Appl. Surf. Sci. 504 (2020) 144347.
[53] B. Tahir, M. Tahir, M.A. Che Yunus, A.R. Mohamed, M. Siraj, A. Fatehmulla, Appl. Surf. Sci. 520 (2020) 146296.
[54] M. Tahir, B. Tahir, Z.Y. Zakaria, A. Muhammad, J. Cleaner Prod. 213 (2019) 451–461.
[55] F. He, B. Zhu, B. Cheng, J. Yu, W. Ho, W. Macyk, Appl. Catal. B 272 (2020) 119006.
[56] J. Fu, Q. Xu, J. Low, C. Jiang, J. Yu, Appl. Catal. B 243 (2019) 556–565.
[57] H. Rongan, L. Haijuan, L. Huimin, X. Difa, Z. Liuyang, J. Mater. Sci. Technol. 52 (2020) 145–151.
[58] Q. Xu, L. Zhang, B. Cheng, J. Fan, J. Yu, Chem 6 (2020) 1543–1559.
[59] Q. Xie, W. He, S. Liu, C. Li, J. Zhang, P.K. Wong, Chin. J. Catal. 41 (2020) 140–153.
[60] Q. Li, W. Zhao, Z. Zhai, K. Ren, T. Wang, H. Guan, H. Shi, J. Mater. Sci. Technol. 56 (2020) 216–226.
[61] F. He, A. Meng, B. Cheng, W. Ho, J. Yu, Chin. J. Catal. 41 (2020) 9–20.